Constructing and commissioning of a Multi-Grid neutron detector prototype for the European Spallation Source

From welding to detection

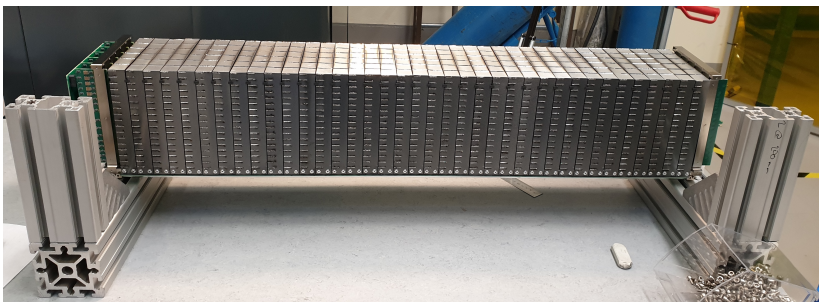

Rebecka Wahlén

10th June 2022

Abstract

A prototype of a novel ^{10}B-based neutron detector called the Multi-Grid detector has been constructed, tested and commissioned for the European Spallation Source (ESS). The detector is constructed after the specifications set by the CSPEC instrument at ESS and is therefore called the CSPEC Multi-Grid detector. The detector uses multiple layers of solid coating containing $^{10}B_4C$ on the edges of a voxelated proportional counter gas detector. The detector was constructed at the ESS detector workshop Utgård in Lund. Initial tests were also performed at Utgård to ensure the functionality and initial state of the detector. It was then moved to the Source Testing Faculty at the Division of Nuclear Physics at Lund University to test the detector with moderated neutrons and with gamma-rays from radioactive sources. Lastly the detector was commissioned at LET, ISIS, for comparison between the detector and the ^{3}He detectors used in the LET instrument. The tests performed in Lund demonstrated that the Data Acquisition System (DAQ) of the detector and the detector itself was functioning, a discrimination threshold for discriminating gamma-rays was found, as well as that the detector is sensitive to neutrons. The tests performed in LET confirmed that the detector can be used for time-of-flight measurements in the energy range required by the CSPEC instrument, furthermore both line-shape and signal to background ratio of the CSPEC Multi-Grid detector was comparable to the ^{3}He detectors.

Acknowledgements

I would like to start by thanking my supervisor Hanno Perry for all the help throughout this work. He put me in contact with Ramsey Al Jebali from the detector group at ESS, making the project possible to begin with. He especially helped early on introducing me to the command line and helped me install Garfield ++. He has also helped a lot with this paper.

I would also like to thank my secondary supervisor Ramsey Al Jebali for making this work possible to start. He has helped me a lot, especially in the construction and testing part of this work.

Alexander Backis also deserves a big thanks. He helped me a lot throughout the building and testing process. He had prepared code used for previous prototypes of the Multi-Grid detector which I could build on top of which helped out a lot.

I would like to thank the detector group at the ESS for allowing me to help with the construction of the detector, and being a part of testing it. Special thanks go to Alessio Laloni for teaching me how to point weld and use a soldering iron.

I would also like to thank the members of Nuclear Physics at Lund Universety. Special thanks go to Kevin Fissum and Nicholai Mauritzson for helping to set up the detector at the STF and showing a lot of interest in the testing of the detector.

Popular science summary

Similar to the way X-rays can expose the atomic structures in the body, revealing broken bones, neutrons can be used to expose the nuclear composition of matter. A vital yet challenging part of using neutrons in science is to detect them. In this work a neutron detector prototype based on a novel technique has been constructed, tested and commissioned.

Neutrons are uncharged particles with about the same mass as protons. Due to its lack of electrical charge it will almost exclusively interact with the nuclei of the atoms it encounters. This means that neutrons can be used to study materials on a nuclear level. However, since the nuclei radius only spans a factor 0.0001 of the radius of an atom, the neutron can encounter a lot of atoms before it hits a nucleus allowing deep penetration into sample materials. This either means that the neutron has to encounter a lot of atoms to increase the likelihood of an interaction, alternatively to use more neutrons so that there are more neutrons available to hit the nucleus.

This creates the need for neutron sources that can provide **a lot** of neutrons. One facility that will produce an unprecedented number of neutrons is the European Spallation Source (ESS), which is still under construction at the time of writing this paper. ESS is a neutron source placed at the outskirts of Lund and will be one of the neutron facilities creating the most number of neutrons per second when it is up and running.

When studying nuclei with the help of neutrons, the path and velocity of the neutron before and after colliding with nuclei are vital. Imagine a billiard ball. If the billiard ball hits the edge of the billiards table it will bounce out with the same angle, however mirrored, and same velocity as it entered with. If the billiard ball instead hits another billiard ball the path will be harder to anticipate. It will however not exit with the same, but mirrored angle and same velocity as it initially had. Information about what the billiard ball has collided with can therefore be gained from looking at the path and velocity before and after the collision. The same is true for neutrons colliding with nuclei.

If the path and velocity of the neutron is known before and after the interaction with a nucleus, information about the collision can be gained. This information on the collision can in turn give information on properties of the nuclei collided with. To determine the exiting path of the neutron a neutron detector must be used. This is not straightforward since the neutrons, as described above, can travel far before interacting with any nuclei. The goal of this work was to construct, test and commission a novel state-of-the-art neutron detector prototype called the CSPEC Multi-Grid detector for the ESS.

The prototype detector was built at the ESS detector workshop Utgård in Lund. It was first tested at Utgård and at the Source Testing Facility at Lund University. The initial tests showed that the electronics used, and all parts of the detector were working

as expected. The detector was then sent to the LET instrument at ISIS, a facility in UK similar to ESS, to compare its performance to another well-established neutron detector type, the ^{3}He detector. The detector clearly detected neutrons even after the long transport to the UK!

Contents

1 Introduction

The European Spallation Source (ESS) is a neutron facility outside of Lund to be opened for users by 2027. When up and running it will be the brightest neutron source to date. The neutrons at ESS will be used to provide advancements in a wide range of applications, such as computer chips, batteries, drugs, superconductors and how DNA sustains life on a molecular level.

At ESS this will be done through using neutrons to probe different material properties on a nuclear level. Neutrons are general highly penetrating, which means that neutrons can be used to probe bulk samples as well as layered samples. Neutron interactions can also be nondestructive, meaning even delicate samples can be studied without destroying them. This also means that several measurements can be performed on the same sample. Neutrons can also be used for studying dynamic properties of molecules.

ESS will have 22 instruments, all constructed to take advantage of different neutron properties. One example is the CSPEC instrument which is a cold chopper direct geometry time-of-flight spectrometer instrument planed for the ESS that will use inelastic coherent scattering to determine structures and dynamics of samples in-situ. However, to be able to study anything with neutrons they have to be detected. That neutrons in general are highly penetrating in matter makes neutron detection difficult.

A well-established neutron detector is the ^{3}He detector, using that thermal neutrons have a high probability to be captured by ^{3}He. However, due to the ^{3}He shortage the price of these detectors has risen significantly, resulting in a novel detector system is being favored for CSPEC instrument. This novel detector system is to use layers of ^{10}B to detect neutrons [1]. One candidate for ^{10}B layer detector is the Multi-Grid detector. The Multi-Grid detector uses the same principles as gas detectors uses to detect charged particles, together with layers of $^{10}B_4C$ which captures thermal neutrons and results in charged particles which are detected. Several parallel layers of $^{10}B_4C$ are put after each other to obtain an neutron detection efficiency matching the ^{3}He detector. The Multi-Grid detector is voxelated creating a 3D position resolution for the detected neutrons, which is important for the science to be performed with the CSPEC instrument.

There are previous versions of the Multi-Grid detector. The first was built at ILL, from which several more have been constructed, however built for different neutron facilities. Therefore, to be able to use a Multi-Grid detector setup for CSPEC, a novel prototype designed for CSPEC has to be constructed and tested. One of the final prototypes to be constructed is the CSPEC Multi-Grid detector. The performance of this detector has to be tested and evaluated for how well it performs with respect to the specifications set by CSPEC.

1.1 Scope and aim of this work

The aim of this work is to construct, test and commission the CSPEC Multi-Grid detector.

The construction part will include cutting and evaluating Gd_2O_3 shielding as well as fixing shielding to the aluminum back pieces of the grids. The grids are to be assembled and welded, as well as fitted into a detector structure. The wires are then to be soldered into place. The details of the construction process is described in chapter 4.

When the detector is constructed it is to be commissioned through a series of tests. The functionality of the data acquisition system is to be determined. Characteristics of the detector, as well as the functionality is also to be determined. A gamma-ray threshold calibration to resolve a discrimination threshold for gamma-rays is to be performed. The main objective is to test if the detector detects neutrons. The experimental setup of the tests is presented in chapter 5 and the analysis of measurements performed with the setups is described in chapter 6.

After the initial testing the detector is to be sent to the LET instrument at ISIS for further testing. The goal is to compare the CSPEC Multi-Grid detector to the ^{3}He detectors used at the LET instrument. A description of the experiments performed at ISIS together with the preliminary results is presented in chapter 7.

Lastly in chapter 8 a summary over the work together with a conclusion is found. The next chapter is a background theory chapter, followed by chapter 3 where the Multi-Grid detector is presented in detail.

2 Theory

In this chapter the neutron is presented. Its properties, together with scientific uses, neutron sources and neutron detection is discussed.

2.1 Neutrons and their interaction with matter

Neutrons are uncharged subatomic particle, meaning they do not have an electric dipole moment, with the mass 1.008 665 u, the spin 1/2 and the magnetic moment $-9.66\,10^{-27}\mathrm{JT}^{-1}$ [2, p. 6]. All nuclei except hydrogen nuclei, which only consists of one proton, contains neutrons since they are necessary for the nucleus to be stable. Neutrons outside of a nucleus are called free neutron. Free neutrons are unstable, meaning they will decay. They have the half life 614 s and will β decay into a protons, electrons and a anti leptons [3]. All neutrons discussed from this point forward are free neutrons, if not explicitly said to be inside a nucleus.

The fact that neutrons does not have an electric dipole moment means that they, in general, interact with nuclear forces which have a very short range (a few 10^{-15}m). Apart from the nucleus of an atom, neutrons can also interact with unpaired electrons due to their magnetic moment [4].

A type of interaction between neutrons and matter is neutron scattering, here indicating neutrons interacting with nuclei of a sample. Within neutron scattering, neutrons can be seen both as particles and as a wave. For that reason the energy of neutrons is often given by their wavelength. The conversation from the energy E to the wavelength λ is provided by de Broglie

$$\lambda = \frac{h}{m\mathbf{v}} = \frac{h}{\sqrt{2mE}}$$

where h is the Planck constant, $m\mathbf{v}$ is the momentum of the neutron and m is the mass of the neutron. The neutrons' wave vector $\mathbf{k}$ is also used where

$$\frac{h\mathbf{k}}{2\pi} = m\mathbf{v}$$

In neutron scattering the neutron can scatter either by elastic scattering (the energy and momentum of the neutron remains constant before and after the interaction) or by inelastic scattering (energy and momentum transfer have occurred between the nuclei and the neutron). The new wave vector of the neutrons after the scattering event is denoted $\mathbf{k}'$ and the so called scattering vector $\mathbf{Q}$ is given by

$$\mathbf{Q} = \mathbf{k} - \mathbf{k}'$$

A scattering triangle showing the scattering vector for an inelastic scattering event is presented in figure 2.1. If it would have been a elastic scattering event the length of $\mathbf{k}'$ would be the same as for $\mathbf{k}$.

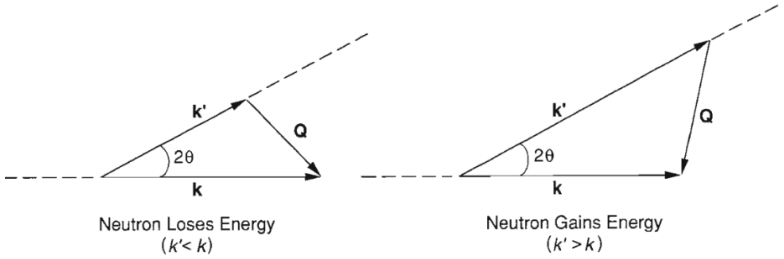

Figure 2.1: The scattering triangle for a inelastic scattering event. To the left the neutron has lost energy, wilte the neutron has gained energy to the right [4].

When using neutron scattering to probe materials the intensity, I, is measured as a funtion of the folowing parameters: energy lost by the neutron ϵ together with the scattering vector $\mathbf{Q}$: $I(\epsilon, \mathbf{Q})$. In 1954 Van Hove showed that $I(\epsilon, \mathbf{Q})$ is proportional to the Fourier transform of a function that describes the probability of finding two atoms with a certain distance between them [4].

In scattering, the interaction can either be coherent or incoherent. In incoherent scattering the neutrons interact with each nuclei separately, without interfering with each other. On the other hand, in coherent scattering the neutrons interact with all nuclei in a sample. There are two forms of coherent scattering, elastic coherent scattering which provides information on the equilibrium structure of a sample, while inelastic coherent scattering provides information on collective dynamic motions, such as vibrational states (phonons), in the sample. When probing phonon properties, the sample can either provide incident neutrons with the energy from a phonon, $h\eta$ where η is the frequencies of the phonon, or take the energy of a phonon from the neutron. The frequencies η is usually around a few 10^{12}Hz resulting in a phonon energy of a few times 4.18 meV, resulting in the energy change ϵ of a few 4.18 meV.

Neutrons can also scatter from unpaired electrons due to their magnetic moment. This is called magnetic scattering and is sensitive to the direction of the magnetization of a sample. It is possible to use inelastic magnetic scattering to probe magnon (magnetic excitation) frequencies, in a similar manner as phonon frequencies can be probed. The magnetic moment is flipped by the inelastic magnetic scattering, thus making it possible to discern magnon from phonon. The intensity $I(\epsilon, \mathbf{Q})$ can be used for in coherent,incoherent and magnetic scattering .

Up to this point the energy of the incident neutrons have not been discussed, it is however an important factor in neutron scattering, as well as other neutron interactions. Neutrons are divided into groups depending on their energy. Thermal neutrons are neutrons with the kinetic energy 25 meV, corresponding to a wavelength of 1.8 Å. Cold neutrons are neutrons with energy less than 5 meV corresponding to 4 Å. Contrastively fast neutrons are neutrons with energy in the range of MeV. Free neutrons often start as fast neutrons as they are freed in nuclear reactions. However, thermal neutrons are often desired for neutron scattering because the wavelength corresponds

to distances between nuclei, which is important for coherent scattering. When using inelastic coherent scattering to probe phonons in the sample it is also important for the initial energy to be of the same range as the transferred phonon energy, to be able to discern the inelastic peak from the elastic peak [4].

The probability of a neutron interacting with a nucleus also depends on the neutron energy. This is described by the cross section σ that has the unit barn [b] which corresponds to $1\,\text{b}=10^{-28}\text{m}^2$. The cross section depends on the nuclei, as well as the energy of the neutrons. Different neutron interactions have different cross section for the same nuclei. There are cross sections for specific interactions to occur, as well as a total cross section of interaction determined by the sum of all the cross sections of specific interactions. For example, the cross sections for elastic and inelastic scattering are different. In figure 2.2 the total scattering cross section for ^{1}H is shown for different energies. This shows that the scattering cross section is constant for neutron energies up to about 100 keV, before decreasing.

Another neutron interaction with matter is neutron capture. In figure 2.2 the capture cross section for ^{3}He, ^{10}B and ^{6}Li is shown for different neutron energies. Figure 2.2 indicates that the cross section of the nuclei decreases with neutron energy (for the specific interactions presented).

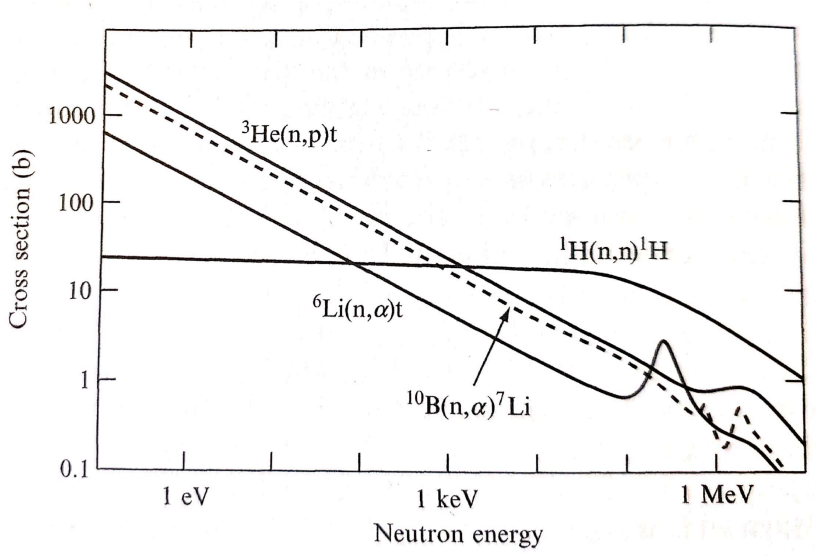

Figure 2.2: The neutron capture cross section for ^{3}He, ^{10}B and ^{6}Li, together with the total neutron scattering cross-section of ^{1}H [2, p. 166].

The cross section is used to determine the attenuation of a neutron beam. Attenuation is defined by how many neutrons from a neutron beam is is diverged from the beam by any type of neutron interaction. A neutron beam with the initial intensity I_0 is attenuated according trough $I = I_0 e^{-N\sigma x}$ where I is the intensity after x m traveled and N is the atomic density. This means that the intensity of the beam reduces exponentially with the traveled length.

The penetration length, here determined by when the beams have reached 37 % attenuation, for electrons, X-rays and thermal neutrons is shown in figure 2.3. The

thermal neutrons have a significantly longer penetration length than both electrons and X-rays, with a few exceptions. The X-rays likewise penetrate furthered than the electron, except for higher atomic numbers.

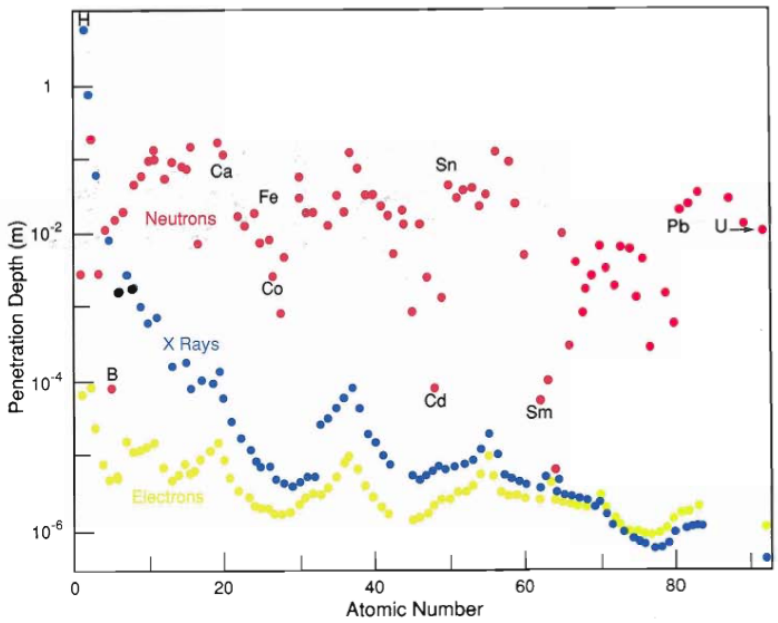

Figure 2.3: The neutron penetration length for neutrons for different atoms (red dots), as well as the penetration length for X-rays (blue dots) and electrons (yellow dots). The penetration length of the particle beams are followed until they have attenuated by 37 % of their original intensity [4]

In contrast to neutrons, a heavy, charged particle, such as the α particle does not in general interact with the atomic nuclei. Instead it loses kinetic energy through Coulomb interactions with atomic electrons. Due to it being a heavy particle, a single, much lighter electron does not change its energy significantly, resulting in many interactions being necessary to stop it. This leads to ionization of the material along the path it travels through. The energy loss per distance traveled for charged particles is described by Bethe-Bloch formula. This states that the energy loss per distance traveled is proportional to $\frac{1}{v^2}$ where v is the velocity of the charged particle. This is also true for lighter, charged particle, such as electrons. Electrons also interact through Coulomb interaction with with atomic electrons. The lighter mass leads to much higher velocities for the electron compared for the α particle. This means that the energy lost per distance traveled is much smaller, resulting in a longer distance traveled before being halted [2, p. 129-135]. The penetration length for electrons for different materials is shown in figure 2.3.

Another particle that interacts with the atomic electrons are photons. Photons generally penetrate further than electrons, as presented in figure 2.3. For photons with energy below about 0.1 MeV the most common type of interaction is photoelectric absorption which entails a complete loss of energy to an inner atomic electron, releasing it from the atom. For energies between about 0.1 MeV to 10 MeV the most common type of interaction is Compton scattering. This entails a partial loss of its energy to an outer atomic electron, resulting in a scattered photon with lower energy than the

initial photon together with a free electron. A photon can be Compton scattered several times resulting in a multitude of electrons before it is photoelectrically absorbed [2].

2.2 Neutron sources

Despite being abundant inside the nuclei, free neutrons are rarer in nature. One exception is secondary particles from cosmic rays. Cosmic rays are either nuclei or electrons that originates from outer space, as well as from the sun. When these particles (called primary rays) enter the outer edge of the earths' atmosphere they interact with atoms creating secondary particles. These secondary particles can be a wide verity of particles, such as neutrons and muons, and can be observed on ground level [5].

It is also possible to obtain free neutrons from nuclear reactions. One example is the ^{141}Am/^{9}Be (Am/Be) source. ^{141}Am is radioactive with the half-life of 432.2 years. The decay products are α particles with the average kinetic energy of 5.5 MeV. The ^{9}Be is itself stable, however when interacting with an α particle it can create a fast neuron together with a ^{12}C nuclei. The fast neutrons are accompanied by a 4.44 MeV gamma-ray in about 60 % of all cases from deexcitation of the ^{12}C. The decay of ^{141}Am is also associated with released gamma-rays with the energy 60 keV [6].

Another neutron source is the spallation source. In spallation a highly energetic particle, like a proton, collides with a target nucleus. This particle reacts wite the nucleons inside the target (the protons and neutrons). This results in an intranuclear cascade of high energy nucleons and pions within the nucleus. Some of these nucleons and pions escape the nucleus, while others leave their energy to the nucleus, resulting in the nucleus being left in an excited state. The nucleus deexcite by evaporating lower energy nucleons as well as α particles and other particles, although the majority of the evaporated particles are neutrons. The high-energy particle that escaped the nucleus can continue and cause more spallation events. The evaporated neutrons main source of neutrons in the spallation event [7].

Neutrons are also created in fission reactors. In fission a thermal neutron is captured by a fuel nucleus, for example Uranium, resulting in a fission event. The fission fragments are two, often unstable, daughters together with 2 to 3 neutrons as well as gamma-rays [2, p. 263-276]. In a scientific reactor an access amount of neutrons are created, in regards to keeping the fission chain reaction going, and extracted from the reactor. This provides a continuous stream of neutrons [4].

All of the sources described above are fast neutron sources, due to the energy released in the underlying nuclear reactions. If thermal or cold neutrons are sought, the neutrons have to be cooled down. This is done through a process called moderation. Moderation of neutrons is based on a neutron scattering in a material, leaving part of its energy in every scattering event. Depending on what material is used the neutron loses different fractions at every scattering event. Due to ^{1}H having approximately the same mass as the neutrons, the neutrons can lose most of its energy in one interaction. This

does however not always happen, for a 2 MeV neutron to be thermalized it takes on average 18 scattering events in ^{1}H [2, p. 144-148]. Common moderation materials are water and liquid ^{1}H. Moreover, since the nuclei in a matter in general are not fixed, but have dynamic movement depending on their temperature, the final energy of the neutron tends to match the atomic energies in the moderator. In room-tempered water this is about 25 meV (thermal neutrons) and in liquid ^{1}H at 20 K this is 5 meV (cold neutrons) [4].

2.3 Science using neutrons

As discussed above, thermal neutrons are in general highly penetrating. This means that to be able to use neutron scattering to probe inter-nuclear distances, as well as dynamic properties of matter, high fluxes of neutrons have to be accessible. Bright neutron facilities are therefore necessary to advance our knowledge in this area.

One research facility that will use spallation to obtain free neutrons is the European Spallation Source (ESS). It is under construction outside of Lund at the moment of writing this report and is estimated to be in operation for users in 2027 [8]. Through the linear accelerator protons are accelerated into 2.86 ms long pulses with the velocity 98 % of the speed of light. A new pulse is created every 71 ms [9]. The target is a stainless-steel disk containing tungsten bricks. The disc rotates with a speed of 23.3 RPMs and is cooled by liquid helium. The tungsten nuclei spallates high energy neutrons, together with other particles, when bombarded with the proton pulses. The neutrons are moderated by a hydrogen and water-based moderator and beryllium-lined reflectors and transported to the instruments through neutron beam lines [10]. A total of 22 different neutron instruments are foreseen at ESS [11].

The resulting pulse shape after the moderator is shown in figure 2.4. As can be seen the ESS pulse will provide a larger amount of neutrons in total, even if the accelerator is only run at 2 MW. This longer higher pulse will result in ESS becoming 100 times brighter compared to excising neutron research facilities.

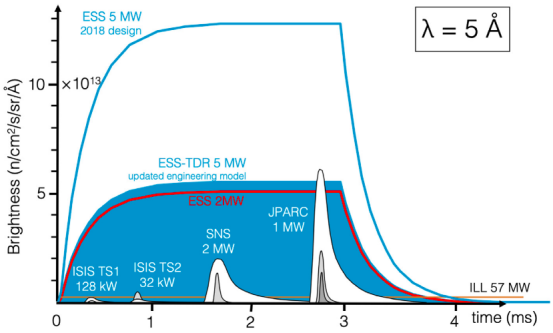

Figure 2.4: The brightness of the moderator at a wavelength of 5 Å. The blue line shows one version of moderator, while the blue filled pulse shape shows a newer design of the moderator. The red line shows the pulse from the accelerator only running on 2 MW, instead of the possible 5 MW. As a reference other pulses from other spallation sources are shown, including JPARC (Japan), SNS (USA), ISIS (UK). The reactor source ILL is also displayed as a reference [11].

A way to determine neutron energy in a spallation facility is to use time-of-flight. If the traveled distance of a neutron, together with the time it took for the neutron to travel this distance, is known, the velocity is calculable. From the velocity the kinetic energy can be determined.

CSPEC, a cold chopper direct geometry spectrometer instrument, will be one of the early instruments deployed at the ESS. It will use time-of-flight together with a large area detector to probe inelastic coherent scattering. A special case not previously discussed is quasielastic neutron scattering (QENS) where the transferred energy in the scattering interaction is very small. QENS can be used to study hard condensed matter, typically magnetism or functional materials. The resulting peaks from motions in the matter will be close to the elastically scattered neutron peak. For this reason, it is important to keep the signal to background ratio high, as well as understanding the background well so that even small peaks can be discernible. At CSPEC the signal to background ratio is required to be 10^5 for the incident neutron wavelength 5 Å. The energy resolution of CSPEC will be given by the smallest transferred energy discernible from an elastic scattering event. This can be determined from the wavelength uncertainty $\Delta\lambda$ from the incident neutron beam. In CSPEC $\Delta\lambda$ =1.72 Å. Inelastic scattering outside of the QENS regime will be used to study novel states of matter, which in turn are expected to be used in topological quantum computers.

CSPEC will be require the extraction neutron wavelengths between 2 Å and 20 Å, corresponding to 20.25 meV to 0.2025 meV. Specific wavelengths in this range will be provided through the cold-chopper system. The cold-chopper systems absorbs all other wavelength not desired creating a well defined entering time of the neutrons. The detector setup shall cover 170° in the equatorial plane and ±26.5° of the vertical plane. The detectors is placed 3.5 m from the source, this means that the detectors will cover an area of 30.6 m^2 [12]. This large area detector setup is necessary to be able to probe several regions of scattering vector **Q** simultaneously. The sample area at CSPEC is shown in figure 2.5, including the sample pot where the sample will be housed, the neutron entrance, the beam dump, the collimators which will absorb

re-scattered neutrons as well as the detectors housed in their vessels.

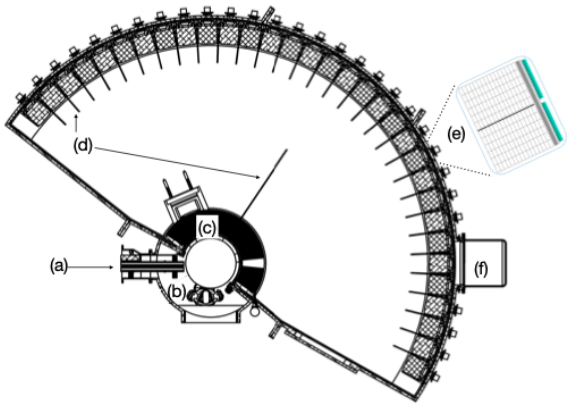

Figure 2.5: (a) indicates end of neutron beam guide and the entering point of the neutrons. In (b) the top view of a person inside the sample environment pot is shown. In (c) the collimator is indicated. (d) show the detector collimation vanes. In (e) the detector vessel is shown together with a zoomed image of the two detector columns housed in one vessel. The columns have a neutron absorption vane indicated by the black line. Lastly (f) show the beam dump [12].

The detectors used shall provide a 3D position of the detection of the scattered neutrons. From this detection position together with the detection time the time-of-flight of the neutron can be determined. An initial time and position of the neutrons before they have interacted with the sample is provided by the chopper system. The energy (wavelength) is also, known with $\Delta\lambda$ =1.72 Å, before the interaction, providing the initial wave vector $\mathbf{k}$. The final wave vector $\mathbf{k}'$ can be determined from the position and time from the detector system, resulting in scattering vector $\mathbf{Q}$ being obtainable.

2.4 Neutron detectors

As discussed, a large area detector setup is to be used at CSPEC. A common base for thermal and cold neutron detectors are gas detector. These do not detect neutrons directly, instead they detect products from neutrons interacting inside the gas detectors. Gas detectors are as the name suggests filled with gas. Charged particles, such as α particles, ionize the gas atoms resulting in free electrons and ions. With the help of an applied electric field the resulting electrons will be accelerated to an anode and the positively charge ions to a cathode. This results in a pulse in both the anode and the cathode. In the case of a proportional counter the applied voltage is large enough for the accelerated electrons to cause further ionization in the gas. This creates an amplification of the original pulse resulting in a higher signal that is proportional to the original ionization from the charged particle. How much the signal is multiplied is called the gain [2, p. 152-155]. An example of how a proportional counter gas detector can look can be seen in figure 2.6.

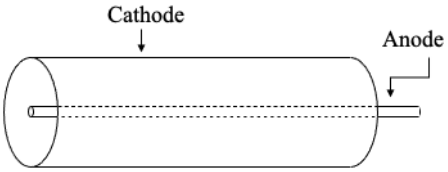

Figure 2.6: An example geometry of a proportional counter gas detector. The shell of the cylindrical detector is grounded, alternatively negatively charged, and work as a cathode for the detector. The wire has a high voltage applied to it and functions as an anode for the detector. Between the shell and the wire the gas is housed.

As seen in figure 2.2 both ^{3}He and ^{10}B have large capture cross sections for low energy neutrons. ^{3}He is a common choice of material for neutron detection. ^{3}He capturing a neutron results in the reaction ^{3}He(n,α)^{1}H with the Q value 0.764 MeV which is divided between the α particle and the ^{1}H. The charged capture products will ionize the gas that results in an electrical pulse. For previous large area detector setups, ^{3}He have been used, however in the latest years the availability of ^{3}He has started to run low, resulting in increased prices. For this reason an alternative is sought to be used at CSPEC [1].

Thermal neutrons also have a high capture cross-section with ^{10}B (although about 40 % lower than ^{3}He). The thermal neutron being captured by ^{10}B is described by the reaction ^{10}B(n,α)^{7}Li. The resulting Q value is 2.79 MeV, however the Li nuclei is left in an 0.48 MeV exited state in 94 % of the times. The resulting kinetic energy is therefore 2.31 MeV most of the time. This energy is divided between the α particle and the ^{7}Li nuclei. The α and the ^{7}Li nuclei will divide the energy according to Newtons third law, this means that the total momentum of the system is constant. This means that the α and the ^{7}Li will gain the same amount of momentum but in opposite directions, since the cold neutron has very little momentum to start with, the system has close to no momentum before the reaction. This means that the α will have the energy 1.47 MeV and the ^{7}Li will get 0.84 MeV. The excitation in the Li nuclei will deexcite via the emission of a 0.48 MeV gamma-ray. The resulting capture products are detectable in a gas detector.

In contrast to ^{3}He, ^{10}B is not a gas in room temperature and can therefore not be mixed into a gas detector directly. One possibility is to coat the edges of a gas detector with ^{10}B. The thermal neutron is the captured by the ^{10}B inside a coating on the side of the detector. Either the α particle or the Li nuclei reaches the gaseous region of the detector, ionizing the gas atoms, while the other is emitted into the opposite direction and deposits is energy inside the coating itself. A type of detector using this reaction is the Multi-Grid detector described in the next chapter.

3 The Multi-Grid neutron detector

In this chapter the Multi-Grid detector is described in detail. First the general principles of the Multi-Grid detector is presented. The different prototypes are discussed, followed by the introduction of the Multi-Grid detector constructed for the CSPEC instrument, the CSPEC Multi-Grid detector.

3.1 Geometry and detection principle

As described in section 2.4 the sides of a gaseous detector can be covered with ^{10}B to detect thermal neutrons. This is used in the Multi-Grid detector. The Multi-Grid detector uses layers of $^{10}B_4C$ to capture thermal neutrons. If the $^{10}B_4C$ layer is to thick the ^{7}Li and α particle cannot penetrate the $^{10}B_4C$ layer, resulting in the neutron not being detected. Therefore it is important to use several layers thinner of $^{10}B_4C$. So called grids, shown in figure 3.1 (a), built from $^{10}B_4C$-coated aluminum blades are therefor used. The normal blades, indicated with blue lines in figure 3.1b (b) are $^{10}B_4C$-coated on both sides, creating 33 layers of $^{10}B_4C$ in the case of the grid shown in 3.1. The resulting efficiency of the detectors capability depends on the thicknesses of the $^{10}B_4C$ layers. The radial blades indicated by green lines in 3.1 (b) can also be coated with $^{10}B_4C$ to decrease internal neutron scattering. In the back of the grid a red line indicates the presence of some shielding, preventing neutrons that has not been captured by the layers of $^{10}B_4C$-coating from back scattering.

The aluminum blades in the grids form square tubes, also called voxels. One voxel is indicated in figure 3.1 (a). The grid in figure 3.1 contains 6x16 voxels of the size 2.5x2.5x1cm^3. The design of the grids, as well as the thickness of $^{10}B_4C$-coating and numbers of created tubes vary with type of Multi-Grid detector.

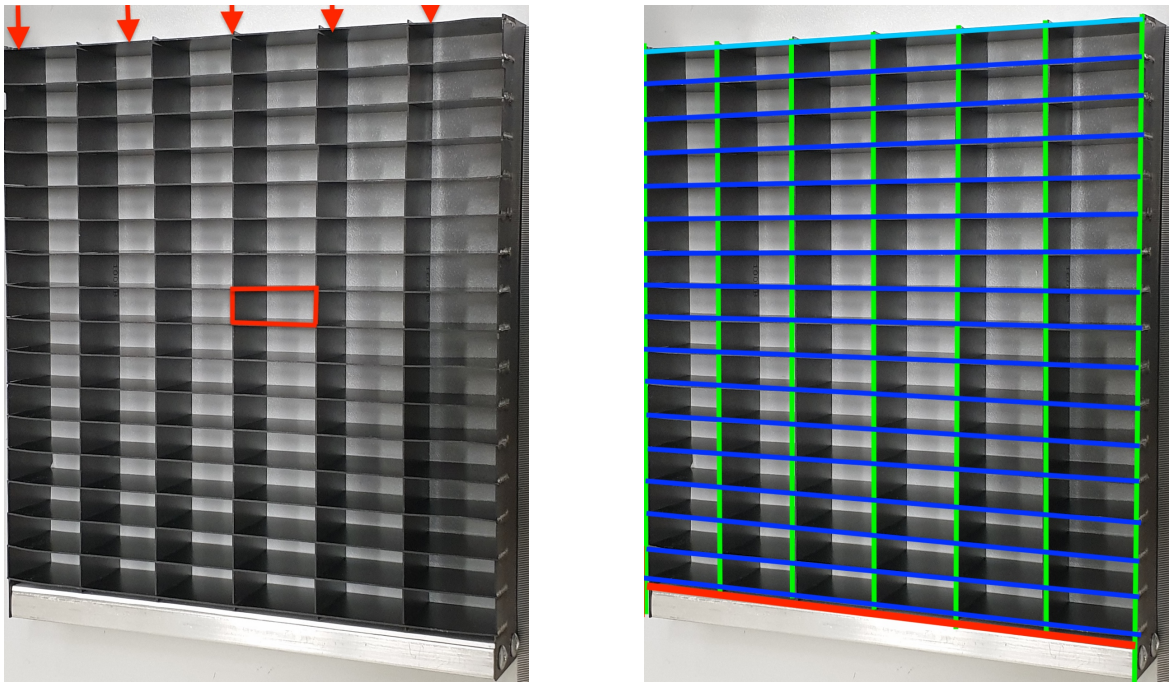

(a) **(b)**

Figure 3.1: (a) an example of a grid used in a Multi-Grid detector. One voxel of the grid is indicated with a red square, and the direction of incident neutrons is indicated with red arrows. This grid us used in the CSPEC Multi-Grid detector introduced in section 3.3. (b) shows the same grid with color coded markings. The green lines show the radial blades and the blue lines show the normal blades. All radial blades have the same 2 μm $^{10}B_4C$-coating on both sides. The normal blades are coated on both sides with the same thickness, except the first blade, light blue in the image, which is only coated on the side facing the rest of the grid. The normal blades have 2 different thicknesses, 0.65 and 1.15 μm, of $^{10}B_4C$-coating to optimize the neutron efficiency. The red line shows the Gd_2O_3 shielding placed on the aluminum brick of the grid.

One voxel from a grid is shown in figure 3.2 (a). In the Multi-Grid detector several grids are stacked after each other, electrically isolated from each other, resulting in longer square tubes. A longer tube is indicated in figure 3.2 (b), here containing 6 voxels in total. Each long tube contains a centered wire, this is also shown in 3.2. The wire is subjected to High Voltage, while the grids separately are grounded. The grids therefore functions as cathodes while the wires function as anodes.

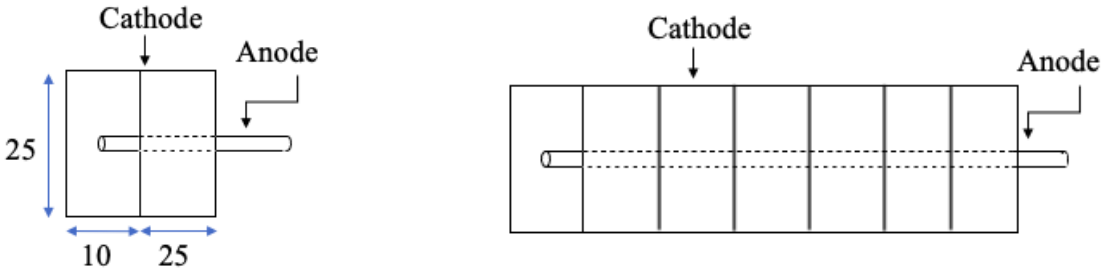

(a) **(b)**

Figure 3.2: A single voxel (a), as well as a series of 6 voxels in parallel (b) representing having 6 grids placed in parallel. The size of the voxel in mm is shown in (a). A wire is situated in the center of each voxel (here described as an anode), while each grid works as a cathode. The size of the square tubes varies with different Multi-Grid detector, in this figure the CSPEC Multi-Grid detector is used as an example.

The stacked grids are housed inside an aluminum vessel. The aluminum vessel is gas filled creating several parallel gas tube detectors from the tubes created by the grids together with the centered wires. Compare figure 3.2 to 2.6. Each voxel in the Multi-Grid detector functions as a separate gas detector. The geometry of the stacked grids inside its housing vessel is shown in figure 3.3. Different Multi-Grid detectors stack different number of grids, and the housing vessels varies in shape and size. The gas used in the detectors also varies.

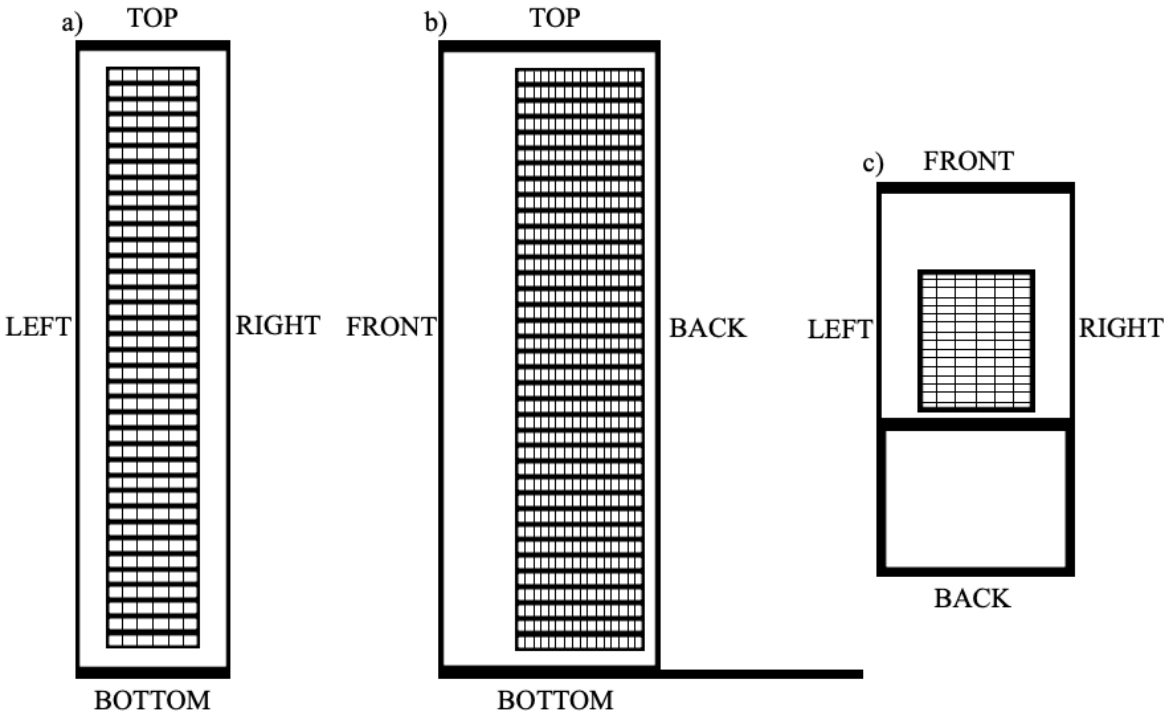

Figure 3.3: The geometry of the detector inside the vessel. This is the geometry for the CSPEC Multi-Grid detector. In a) a cross section seen from the front is shown. All 37 grids can be seen from grid number 1 at the bottom to grid number 37 at the top. All 6 rows of wires are shown, from wire row 1 to the left to wire row 6 to the right. b) shows a cross section of the geometry shown from the right side of the detector. It shows all grid numbers from grid number 1 in the bottom to grid number 37 at the top. It also shows all wire numbers from wire number 1 in the front to wire number 16 in the back. c) Shows a cross section of the geometry seen from the top of the detector. It shows all 16 wire numbers from wire number 1 in the front to wire number 16 in the back. It also shows all wire rows from wire row 1 to the left to wire row 6 to the right.

When a charged particle is released in a voxel it ionizes the gas atoms, as described in chapter 2. This results in a signal in the grid and in the wire. The grids are, although electrically isolated, not separated from each other in a way that stops particles from traveling between grids in the same tube. Thus, particles that has been released in one grid can travel into another grid and therefore give signal in several grids. Either way, the position of the voxel where the neutron was captured can be decided from the signal in the grid (or grids) together with the signal in the wire. All voxels positions are known, resulting in a 3D position together with a detection time.

As the neutron capture products are not released directly in the gaseous region, but inside the $^{10}B_4C$-coating. The energy deposited in the gaseous region is not known a priori. The capture products can have deposited most of its energy before they enter and start to ionize the gas atoms. This means that the pulse height spectra will not be as predictable as for a ^{3}He detector. This also means that it is unlikely for both the α particle and the Li to be detected simultaneously. One capture product will travel into the coating layer, and the aluminum blade while the other particle will travel outwards

towards the gas. This means only one of the capture products will be detected. This makes the pulse height spectra for Multi-Grid detectors less straightforward and makes the distinction between neutrons and other possibly detected particles difficult.

The Multi-Grid detector can also detect gamma-rays. All gamma-ray interaction with matter results in free electrons. These free electrons will lose their energy in the same way the heavier, charged particles will. However, electrons lose less energy per distance traveled due to being lighter. This means they will in general lose less energy, resulting in less ionization. For this reason, the gamma-rays are expected to be detected with lower signal in the wire and grid. Charged particles such as electrons and α particles will not penetrate the aluminum vessel and will therefore not be detected.

3.2 Multi-Grid prototypes

Several previous Multi-Grid detectors have been constructed and tested for different neutron instruments.

At ILL several prototypes constructed and tested. An early prototype of the Multi-Grid-detector was the MG-12. This was created using 12 grids, each grid having different thicknesses of the $^{10}B_4C$-coating on the normal blades. In contrast to the grid in figure 3.1 the grids used in MG-12 only had 4x15 voxels each with the dimensions 2x2x1cm^3. From this prototype a longer detector using the same grid design was constructed, the MG-96, which used 96 grids. In the MG-96 the normal blades were coated with 1 μm of $^{10}B_4C$-coating. The next prototype was the MG-IN6, constructed for the IN6 instrument at ILL. The MG-IN6 used the grids from the MG-96, however stacked in 6 columns with 16 grids in each column, instead of the 96 grid column used in the MG-96. Next was the MG-IN5 prototype, constructed for the IN5 instrument at ILL. This had the voxel size 2.35x2.35x1cm^3. 8 columns of 128 grids each was constructed [13].

SNS has also constructed a Multi-Grid prototype for the CNCS instrument, called the MG.CNCS. The grids used in the MG.CNCS used 4x17 voxels, each voxel spanning 2.2x2.2x1cm^3. These grids have varying thicknesses of $^{10}B_4C$-coating on the normal blades to optimize the neutron efficiency. This Multi-Grid prototype was built from 2 columns of 48 grids each [14].

At the ESS detector workshop Utgård a previous prototype of the Multi-Grid detector has also been constructed. The sequoia Multi-Grid detector which was tested at the V20 beamline in Helmholtz-Zentrum Berlin (HZB). The grids in the sequoia detector contains 4x20 voxels of the size 2.25x2.25x1cm^3. One column used 40 grids [15].

In the next section a novel Multi-Grid prototype called the CSPEC Multi-Grid detector is presented

3.3 CSPEC Multi-Grid detector

The CSPEC Multi-Grid detector is built for ESS at the detector workshop Utgård in Lund. It is built for potential use at the CSPEC instrument at ESS, hence the name. The CSPEC Multi-Grid detector, who's grids was shown in figure 3.1 and geometry was shown in figure 3.3, is the main focus of this work. The grids contain 6x16 voxels of the size 2.5x2.5x1cm^3. The voxel size is chosen to obtain the sought **Q** resolution in the CSPEC instrument, together with the time resolution [12]. The detector will contain 37 grids and is built as an intermediate step, using the same readout electronics as the sequoia detector, but with a new grid design. The next prototype built at the detector workshop Utgård in Lund will use the same grid design, however using different readout electronics.

In figure 3.1 (b) the different components of the CSPEC Multi-Grid detector grids are highlighted. The green lines show the radial blades and the blue lines show the normal blades. All radial blades have the same 2 μm boron carbide coating on both sides. The normal blades are all coated on both sides with the same thickness. The first blade, light blue in the image, is the exception as it is only coated on the side facing the rest of the grid. The normal blades have thickness 0.65 or 1.15 μm of $^{10}B_4C$-coating to optimize the neutron efficiency. There are three configurations of the normal blades, the efficiency at detecting neutrons can be seen in figure 3.4. How the efficiency both depends on the capture probability of he neutron, as well as the probability of the capture products being detected [16]. The different configurations are described in Appendix B.

The simulation is made for neutrons hitting the grids at a 90° angle. The required efficiency is above 60 % at the neutron wavelength 5 Å, which the simulation shows for all three configurations plotted.

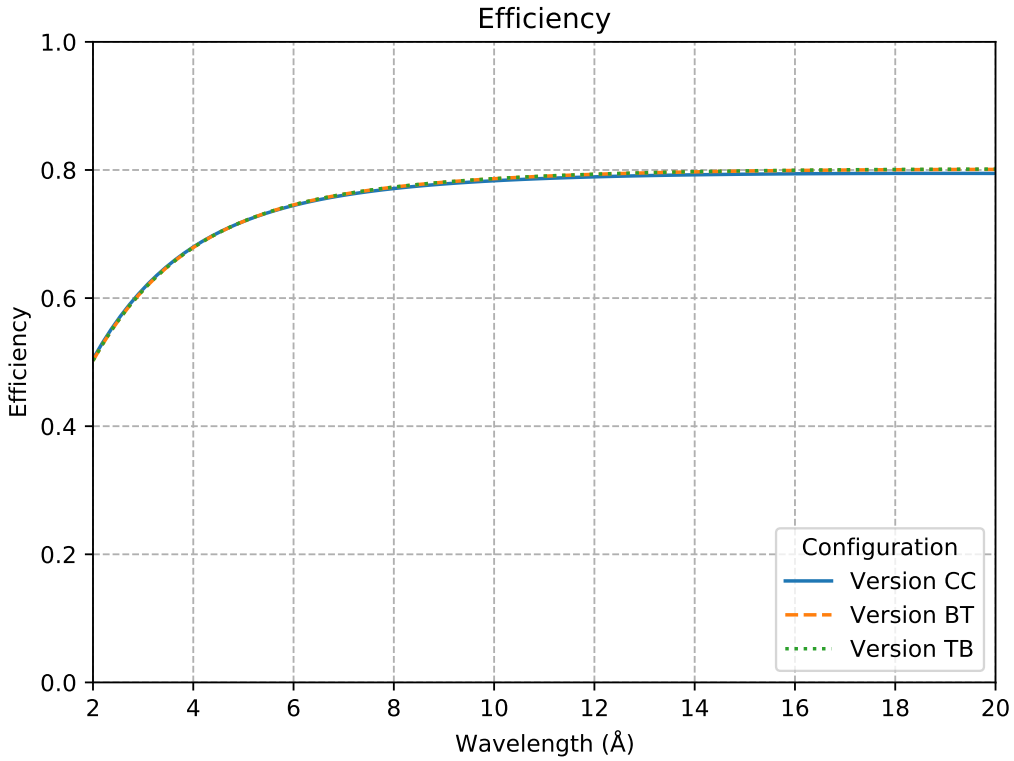

Figure 3.4: The Multi-Grid detector efficiency for the different grid configurations to detect neutrons with different energies. In the different grid configurations the placement of the different thicknesses of $^{10}B_4C$-coated blades are varied slightly. The grid configuration versions are presented in Appendix B. This simulation was performed by Alexander Backis, using the python package found in [17] which is based on [18].

The CSPEC Multi-Grid is a prototype constructed to fit the performance requirements stated by CSPEC. CSPEC, as described in section 2.3, is sensitive to background. It is therefore important to keep the background as low as possible in the detector. One aspect of the background is the scattered neutrons from the aluminum in the detector. These neutrons from within the detector results in an altered time-of-flight measurement. Therefore the radial blades, indicated in figure 3.1 (b), also have $^{10}B_4C$-coating. The idea is that the internally scattered neutron will interact as close to the scattering point as possible to reduce the uncertainty from possible prolonged travel before detection.

In 3.1 (b) the red line shows Gd_2O_3 shielding.The shielding is made of a mix of Gd_2O_3 (74 % by weight) and epoxy. The Gd, especially ^{155}Gd as well as ^{157}Gd, have a large neutron capture cross section, similar to ^{10}B. However the resulting capture products are not charged particle, but gamma-rays [19]. The Gd_2O_3 shielding at the back of the grids prevents neutrons, not captured by the layers of $^{10}B_4C$-coating, from back scattering into the detector. The inside of the vessel is also covered with Gd_2O_3 pieces to reduce detection of internally scattered neutrons. The placement of the Gd_2O_3 shielding inside the vessel is shown in figure 3.5.

(a) **(b)**

Figure 3.5: The vessel seen from the bottom of the detector. (a) show the placement the Gd_2O_3 shielding when the vessel is properly covered with shielding. (b) indicates which of the shielding parts are not in place yet (red marking indicated by the number 1) and which is in place (green marking with the number 2) when only the top of the detector is covered with internal shielding

The detector is built of 37 grids with 6x16 voxels each creating a total of 3 552 voxels. A schematic image of the assembled detector is shown in figure 3.3. The grids are grounded and electrically insulated from each-other and function as cathodes in the detector. The wires are also insulated from each other as well as the grids and are operating at a high voltage of 1.1 kV and function as anodes in the detector. One voxel is shown in figure 3.2 (a) and a series of 6 voxels are shown in figure 3.2 (b).

The detector is filled with a 80/20% gas mixture of Ar and CO_2 by volume. Due to the square geometry of each voxel, the electric field is not straightforward to compute. Therefore, a simulation was performed in Garfield ++, a toolkit made for simulations of detectors using gases or semi-conducting material, to calculate the electric potential of one voxel. Garfield ++ is based on the CERN developed ROOT. The electric potential from a cross-section of a voxel is shown in figure 3.6. Towards the middle of the voxel the electric potential is 1100 V and towards the edges the potential goes to 0 V as expected since the edges are part of the grid, which is grounded, while the center is a wire which has a potential of 1100 V applied to it.

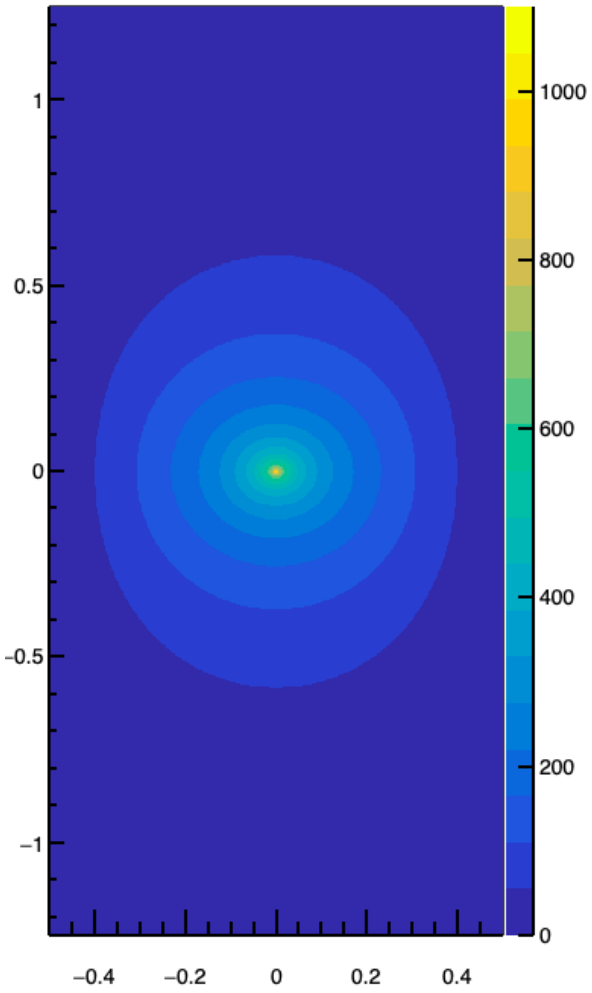

Figure 3.6: The electric potential of a voxel from a grid from a simulation in Garfield ++. The color bar show the electric potential in [V]. The x and y- axes is shown in cm.

The detector is housed in a vacuum-safe aluminum vessel. The detector itself will be operated in a pressure a little higher than atmospheric pressure, while the instrument tank will be in vacuum. The vessel is 4 mm thick in the area where the neutrons are to enter the detector, also called the detector window. Since about 1 % of all neutrons are attenuated by 1 mm of aluminum this means that about 96 % of all neutrons get through the aluminum without getting scattered from their original path. It also means that about 4 % all incoming neutrons will scatter before entering the detector. Outside of the vessel additional external shielding may be used to minimize number of thermal neutrons entering the detector from where the shielding is placed.

The material used for external shielding is called Mirrobor™and is a commercial product, see [20]. The sheets used where 5 mm thick. Mirrobor™has a mass composition of 80 % B_4C and 20 % glue (70 % C, 25 % O and 5 % H). The Boron distribution is 20 % ^{10}B and 80 % ^{11}B, which leads to the total ^{10}B density being $9.4\,10^{21}$atoms/cm^3. Just as the ^{10}B captures the neutrons inside the coating of the grids, the ^{10}B captures the thermal neutrons in the Mirrobor™. The difference is that the charged particles resulting from the capture process is not detected, since the aluminum vessel will stop

them from entering the detector.

3.3.1 Readout Electronics, data format and data analyses

The Multi-Grid detector readout is based on the mesytec MMR Multiplexed Readout electronics [21]. This includes the MMR card on the back of the detector, connected to the card is an optical fibre cable going to a card controller VMMR. Each card is named by a number, called the bus. The controller is connected to the front end of the system, a program on a laptop, from which the charge trigger level and other details are set. Data files are compressed and stored in ZIP-format. In the DAQ software the discriminator threshold is chosen to be at 100 adc which means that everything below 100 adc will not be recorded. This threshold is set to reduce noise. If this threshold is not set high enough all channels will give a signal resulting in large data files containing mostly noise. Due to problems with noise encountered in the grids in previous Multi-Grid prototypes the system only start an event from a wire signal, not from a grid signal.

Data from each card on the back of the detector is connected to a separate bus of the mesytec VMMR controller. Each bus can be operated completely separate with different trigger levels and other options attached to it. The idea is that several detectors can be run simultaneously using the same controller and getting all data in the same zipped file. Each bus have been configured to have 80 wire channels and 40 grid channels.

The resulting data is divided into 32 bit-words where a set of words stores all information for each event. First the header word announces an event is incoming, next comes the data event word with a time stamp, followed by the data-event word which contains the bus, the channel and the charge, here in the form of a adc channel. This is followed by an extended time stamp word which can be used instead of the time stamp provided previously. Lastly the end of event word that announces the end of the event.

In the analyses section, when the data have been read it is transformed to a data-frame element in using Python programming, containing a timestamp, a wire channel (determined by the wire channel that has the highest charge), a wire multiplicity (how many wires have given signal within the event), a grid channel (determined by the grid channel that has the highest charge), a grid multiplicity (how many grids have given signal within the event), wire charge (sum over all wires), grid multiplicity (sum over all grids) and which bus the event had occurred in.

The CSPEC Multi-Grid detector uses two buses to be able to read all 96 wires. To one bus the first 32 wires was connected, while the 64 remaining wires together with all 37 grids was connected to a second bus. This resulted in the 32 first wires not triggering together with the grids located in the second bus. This was due to the fact that only the wires could start an event, and not the grids. This was possible to mend through allowing the grids to trigger as well as the wires after carefully adjusting the grids dissemination threshold.

4 Construction of the CSPEC Multi-Grid neutron detector

In this chapter the construction process of the CSPEC Multi-Grid detector is described. The contribution of the author can be found in Appendix A.

Utgård is a workshop and laboratory of the ESS. The space is shared by the Detector group, the Scientific Activities Division and the Integrated Systeulti Division. It is an industrial warehouse space where detectors are tested and developed for use at the ESS. A point welding station and soldering equipment are available for detector construction. It is at Utgård the CSPEC Multi-Grid neutron detector was assembled.

The first preparation step of construction the detector was to coat aluminum blades with about 1 μm of $^{10}B_4C$ which was done at Linköping for ESS. The next step was to create the Gd_2O_3 shielding sheets, made of 74% by weight Gd_2O_3 and 26% weight epoxy. This shielding was done in-house at Utgård. The ingredients were measured and combined into a paste. The paste was placed in molds and dried overnight in the oven. The shielding sheets were then moved to an aluminum foil to keep cure further for another 4 days. Afterwards, it was cut into strips to fit the back aluminum support pieces for the grids and checked for uniformity an regions that are thinner than the required thickness. The strips that passed the inspection were then glued to the aluminum support pieces as shown in figure 4.1. Lastly the excess shielding was cut of the support pieces with a scalpel.

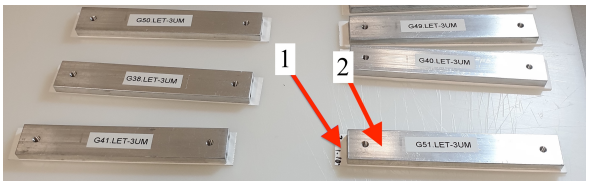

Figure 4.1: The support pieces of the grids with the shielding glued on them. The arrow numbered 1 indicates the Gd_2O_3 shielding, while the arrow numbered 2 indicates the aluminum support pieces for the grids. The support pieces are about 15 cm long and 2.5 cm wide

When the Gd_2O_3 was attached to the back pieces and the blades were delivered from Linköping the grids could be assembled. This was done with the help of a grid jig which holds the aluminum blades in place during assembly of the grids. First the support piece of the grid was placed at the back of the jig. Then the blades were put in place following the different grid configurations that can be seen in Appendix B. A fully assembled grid can be seen in figure 4.2 (a).

Next the grids were welded using point welding. All outer crossing between radial blades and normal blades were welded together to fix the blades to the grids. A figure

of a welded grid can be seen in figure 4.2 (b). After the welding was done the sooth from the welding was cleaned with ethanol and stored until enough grids were welded to assemble the detector.

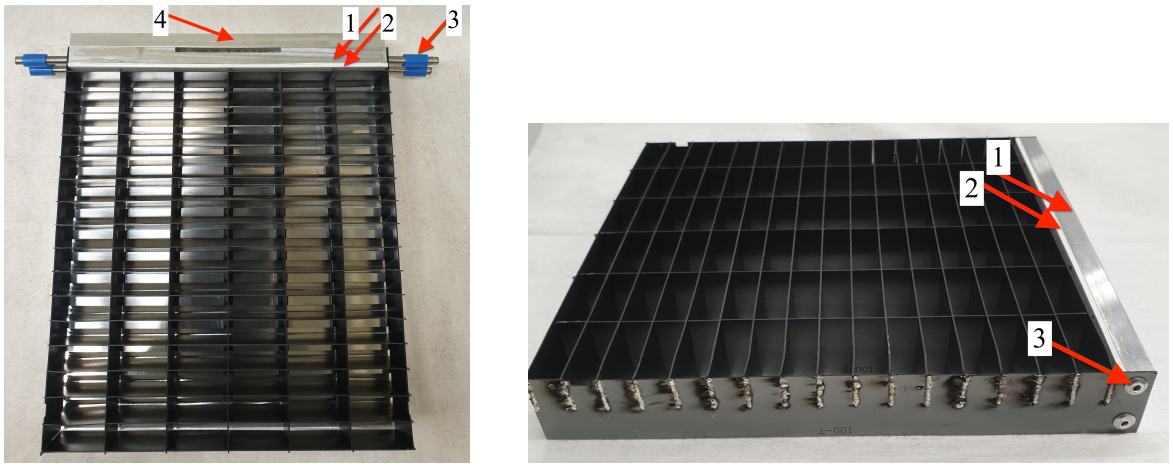

(a) **(b)**

Figure 4.2: A fully assembled grid is shown in (a), before it has been welded together and still in the grid jig. The shielding is facing the rest of the grid (arrow numbered 2), the arrow numbered 3 is pointing to the placeholders for the rivets. Arrow numbered 4 points to the back of the grid jig which the grids are assembled on. Arrow numbered 1 indicates the aluminum back piece of the grids. In (b) a welded grid is shown before it has been cleaned up. The sooth from the welding can still be seen on the side facing the camera. From this angle the rivets fixing the back piece of the grid to the rest of the grid is also visible (arrow numbered 3). Arrow numbered 1 indicates the aluminum back piece of the grid with the Gd_2O_3 shielding glued to it (arrow numbered 2). The scale of a grid is about 15 cm wide and 17 cm long

The first step when assembling the grids into the detector was to fix the grid signal transport PCB onto the detector backbone. The end grids were then placed on the backbone of the detector and an insulating layer was placed on the grid PCB. The assembly process is shown in figure 4.3. The grid PCB is indicated, as well as the insulating layer, the grid backbone and the end grids. Figure 4.3 (a) shows an image of the detector with 17 of the 37 grids assembled. Every grid was screwed on with two screws to the backbone, this is how the grid PCB is connected to each grid. A zoomed in image of how the grids are separated by insulating layer on the backbone is shown in figure 4.3 (b). Due to the separation the grids will be electrically isolated from each-other. Insulating pieces was also placed in the indents towards the front of the grids as shown in figure 4.3 (c) to make sure the separation between the grids are kept. A figure of the fully assembled detector is shown in figure 4.3 (d).

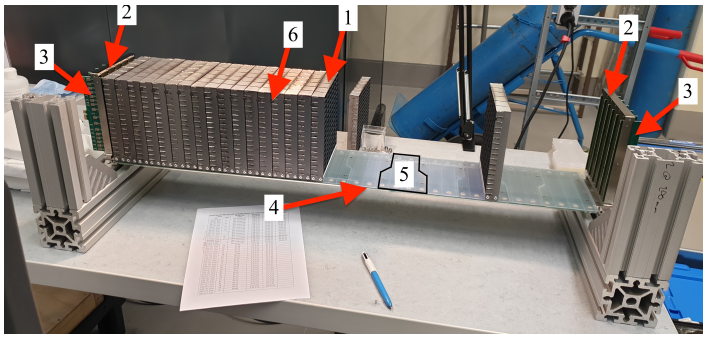

(a)

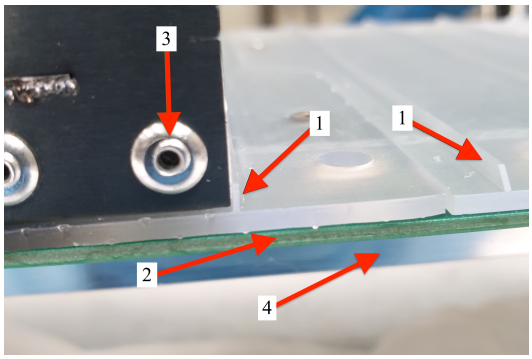

(b)

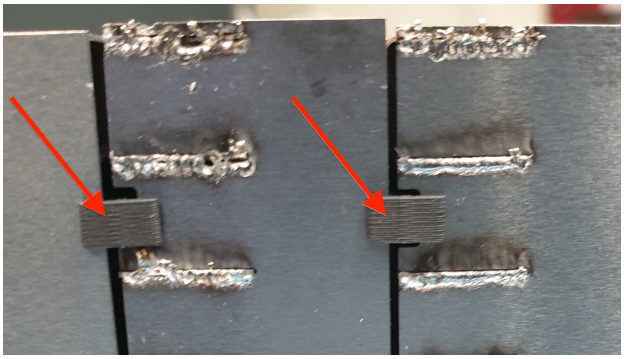

(c)

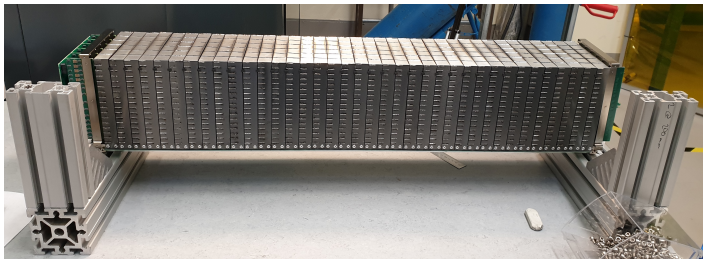

(d)

Figure 4.3: The assembly of the grids in the detector. (a) shows the detector with 17 grids assembled. Arrows numbered 2 show the end grids, where the wire PCBs are indicated by arrows numbered 3. Arrow number 1 indicates one of the grids, and arrow number 6 indicates where the insulating small pieces are placed. Arrow numbered 4 show where the grid PCB is, with the isolating layer placed on top. The shape of the isolating layer is indicated by the black lined shape, surrounding number 5. See pen an A4 paper for scale. In figure (b) the insulation pieces placed on the backbone is shown more closely. Arrow numbered 4 indicates the backbone underneath the grid PCB, underneath the insulation. The insulation both electrically insulates the grids from the grid PCB and the grids from each other. Arrows numbered 1 indicate the separator between the grids. The arrow numbered 3 points to the rivet of the grid and the arrow numbered 2 indicates the grid PCB. In figure (c) the insulating pieces placed between the grids near the front of the grids are shown with the red arrows. This together with the separator on the bottom ensures that the grids will be completely separated, and therefore electrically insulated from each other. Lastly (d) shows the final assembled detector ready to be moved inside its aluminum vessel.

The next step was to solder the wires in place in the detector. The wire was guided

through the detector with a long stick. A weight of 50.2 g was used on one side while the other side was fixed to ensure a constant tension in the wires. The soldering work as well as the PCB copper pads are shown in figure 4.4. When all wires were soldered in place the detector was placed inside its aluminum vessel. The vessel has internal shielding covering the top half of the vessel, as shown in figure 3.5 (b).

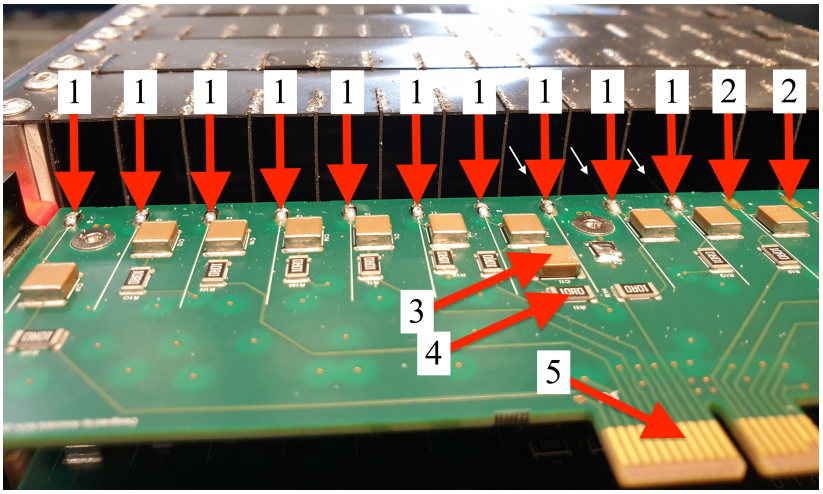

Figure 4.4: Wires soldered in place on a wire PCB. The wire is placed on the copper pad and soldered in place. The high voltage is applied through the copper pads. Arrows numbered 2 show the unsoldered copper pads while arrows numbered 1 show the soldered wires. The white arrows indicate the wires, there are wires on all soldered copper pads, however they are thin so not always visible. The arrow numbered 3 indicates a capacitor which collects the charge from a wire. The arrow numbered 4 indicates a resistor, while the arrow numbered 5 indicates where the wire signals exits the wire PCB.

The vessel was placed on a table with Mirrobor™shielding arcs underneath it. An additional aggregator PCB, placed on top of the wire PCBs, was added to distribute the high voltage and low voltage to the wires, and to transport the wire signals to the interface PCB where the front end MMR mesytec cards are plugged. The gas was connected to the vessel interface and led to the other end of the detector with a pipe. The detector placed inside the vessel before it was closed can be seen in figure 4.5 (a).

On the outside of the vessel the mesytec cards were placed, not connected to anything to begin with, the 80/20 $V\%$ mixture of Ar and CO_2 gas was connected with a gas pipe to a flow meter which was set to about 10 ml/min (not normalized for this gas). The gas was then allowed to flow for 24 hours to fill the detector. Next the MMR mesytec cards were connected to the VMMR-16 mesytec module with optical cables. The HMP4040 rohnde & schwars low voltage power supply was used for the low voltage and the CEAN 4Ch N1471 power supply was used for the high voltage. A figure of the back end of the vessel can be seen in figure 4.5 (b). The high voltage was ramped up from 0 to 1100 V in steps of 50 V.

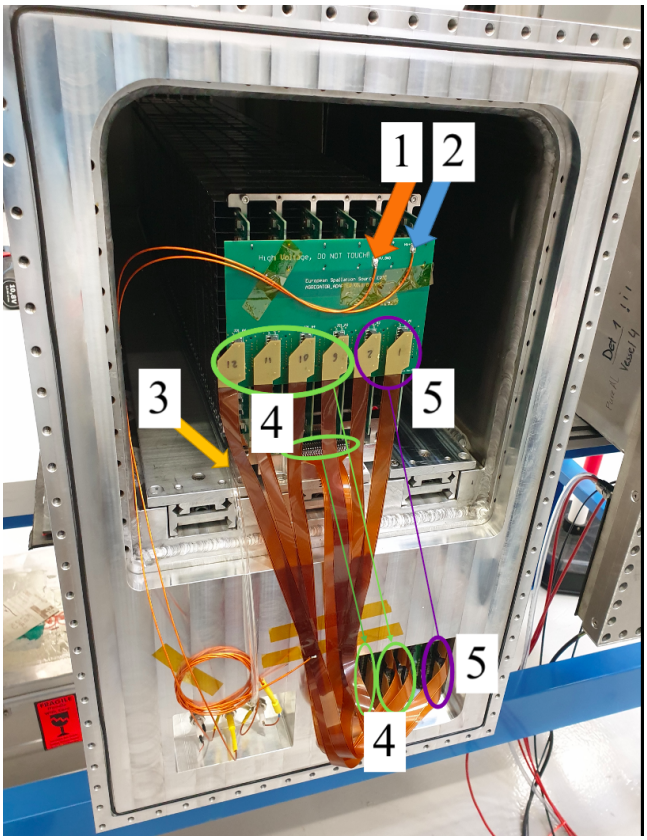

(a)

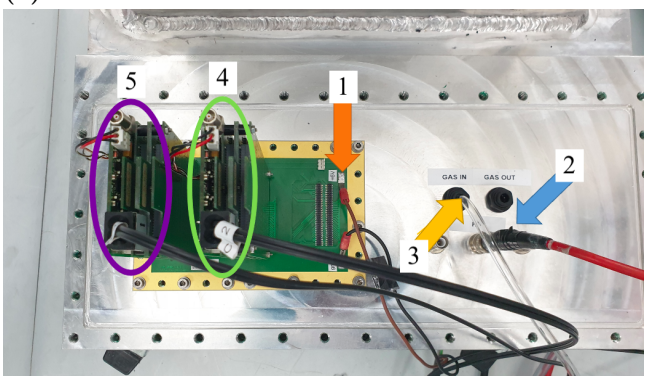

(b)

Figure 4.5: The detector inside the vessel. In (a) the connection from the wires to the vessel is shown from inside the detector. The orange arrow numbered 1 indicates where the low voltage is soldered on the aggregator PCB, and the blue arrow numbered 2 indicates where the high voltage is soldered on. The yellow arrow numbered 3 indicates the gas pipe. How the last two rows of wires (32 wires, wire row 5 and 6) are connected to the vessel is indicated by the purple markings indicated by number 5. How the residual four wire rows (64 wires, wire rows 1,2,3 and 4) as well as the grids are connected from the detector to the vessel is shown with the green markings numbered 4. In (b) the corresponding connections is shown from the outside of the vessel. The orange arrow numbered 1 shows the low voltage connection. The blue arrow numbered 2 indicate the high voltage going into the detector. The yellow arrow numbered 3 indicates the connected gas pipe. Here the mesytec cards are connected to the vessel (green numbered 4 and purple markings numbered 5, this corresponds to the color marking in (a)).

5 Experimental setup

In this chapter the experimental setup of the different measurements performed to test the CSPEC Multi-Grid detector are described.

First a background measurement was taken at Utgård. The goal of the first measurement was to determine early characteristics and possible problems with the detector. Next the entire vessel of the detector was covered with Mirrobor™shielding to minimize any external thermal neutrons from reaching the detector. The purpose of this measurement was to see how much of the observed background at Utgård is caused by the detector components themselves, e.g. possible traces of radioactive material in the hardware of the detector.

The third measurement was performed at the STF to see the response in a radioactively more active environment. It will also serve as a reference for the other measurements performed at the STF. To investigate if the chosen gamma-ray discrimination threshold at 550 adc suitable a threshold calibration was performed with a ^{60}Co source.

With the discrimination threshold calculated from the gamma-ray threshold calibration and initial characteristics of the detector were investigated, the next step was to investigate how the detector behaves when irradiated with thermal neutrons. This was performed with an AmBe source inside a moderator in front of the detector.

5.1 Background studies

Initial tests of the detector were conducted at the detector workshop Utgård to investigate the state and functionality of the detector. Since it is not a radiation-controlled environment the radioactive background is expected to be low, meaning the count rate of the detector should be low for this measurement.

The Multi-Grid detector was placed on a table with the front facing towards the ceiling. Underneath the detector were several layers of Mirrobor™shielding as preparation for further measurement since the detector is heavy it is not desirable to lift the detector unless absolutely necessary. The setup of the detector can be seen in figure 5.1. The data acquisition was started and ran over 50 hours.

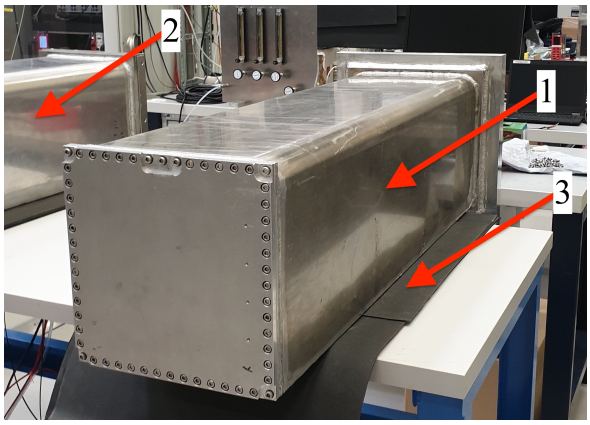

Figure 5.1: The CSPEC Multi-Grid detector placed on a table at Utgård. The detector is indicated by the arrow numbered 1. The back of the detector is facing the table, on which there are several sheets of Mirrobor™. The Mirrobor™is indicated by the arrow numbered 3. The front of the detector is facing towards the ceiling and the top of the detector is closest to the camera. The arrow numbered 2 indicates a previous prototype of the Multi-Grid detector called the sequoia Multi-Grid detector.

To determine what the detector detects when few thermal neutrons are able to enter the detector, Mirrobor™was used to cover the entire detector for the next setup. The Mirrobor™shields thermal neutrons from reaching the detector. The remaining detections are expected to be due to traces of radioactive impurities in the hardware of the detector (could be in the soldering material for example). It could also be from other detected particles, such as fast neutrons and gamma-rays, which are not shielded by the Mirrobor™. In fact, neutron capture in Mirrobor™results realized in gamma-rays which could be detected.

The setup of this measurement is shown in figure 5.2. The detector front is facing the ceiling, while the detector top is facing the camera. For the measurement the data acquisition was started and run for 70 hours.

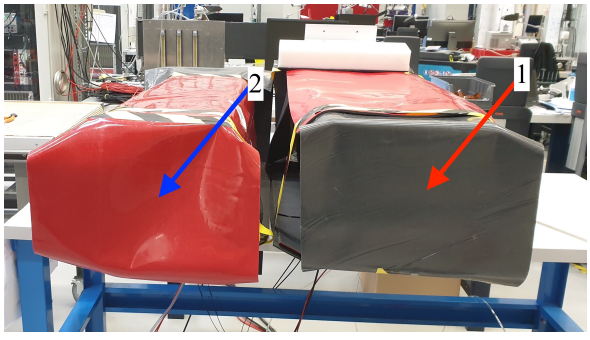

Figure 5.2: The CSPEC multi-grid detector placed on a table with the Mirrobor™shielding all around it to the right (red arrow numbered 1). To the left is the sequoia detector (blue arrow numbered 2).

After conducting the two initial tests at Utgård the detector was regarded to be in a good state and functioning and therefore ready to be moved to the Source Testing Fa-

cility for further testing. The Source Testing Facility (STF) is a collaboration between the applied nuclear physics group at Lund University and the detector group at ESS. It is built to easy access neutron sources for characterisation and development of novel neutron detectors. The STF stores a variety of sources, both gamma-ray and neutron sources [22]. For example, in the aquarium in the back of the STF, a 1.4x1.4m^2 water tank, a PuBe source is stored witch radiates approximately $2.99 \cdot 10^6$neutrons/s [23]. The aquarium is for example used for tagging neutrons.

Furthermore an AmBe source which radiates approximately $1.14 \cdot 10^6$neutrons/s is placed in storage behind the aquarium [23]. The STF also provides a verity of detectors, both gamma-ray and neutron detectors. For example they have ^{3}He detectors. The STF is built to be modular and flexible and stores an extensive set of computers and modules. They also store shielding materials, such as plastic and borated aluminum plates [24]. An example of a study on Beam Monitors that was partially performed at the STF can be found in [25].

The detector was placed inside the STF and the gas, low voltage, high voltage, mesytec cards and the optical fibers were connected as described in chapter 4. The first test performed at the STF was a background study. The detector was placed on the ground, with the bottom of the detector on the floor and the left side of the detector to the aquarium. The position of the detector at the STF can be seen in figure 5.3 and 5.5. The detector was initially flushed with gas for about 24 hours after which the data acquisition was started and run for 15 hours.

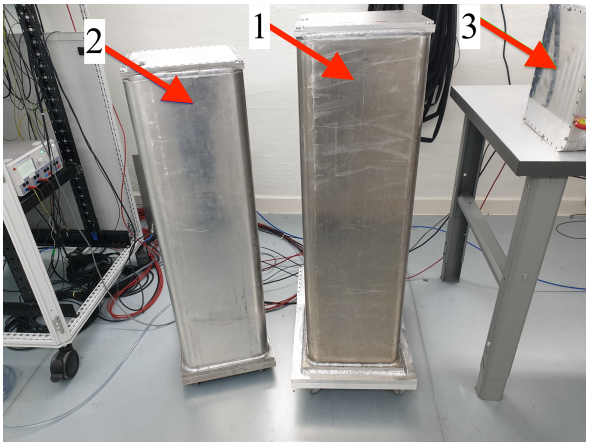

Figure 5.3: The detector placement at the STF. The detector indicated by the arrow numbered 1 is the CSPEC detector. The detector to the left (the arrow numbered 2) is the sequoia detector. The arrow numbered 3 points to the LET Multi-Grid detector which is a bigger version of the CSPEC detector.

5.2 Gamma-ray threshold calibration

In the sequoia Multi-Grid prototype the collected grid charge and wire charge of detected gamma-rays are said to be between 100 adc and 500 adc, and a software discrimination threshold is set at 600 adc to discriminate against gamma-ray defections [15]. For this reason a first discrimination threshold is set to 550 adc for the novel

Multi-Grid prototype. Since the geometries of the voxels are not the same in the two prototypes the electric field will not be the same. This means that the gain for the prototypes might be different, resulting in a different gamma-ray discrimination threshold. This threshold is therefore be tested in the CSPEC Multi-Grid detector to ensure a reasonable discrimination threshold is chosen. A gamma-ray threshold calibration was therefore performed at the STF with a ^{60}Co source.

The ^{60}Co source with the activity 16.64 MBq was placed in front of the detector as shown in figure 5.4. It was placed 19 cm from the top of the vessel, and 16 cm from the left of the vessel. The data acquisition was run for 10 minutes for the measurement.

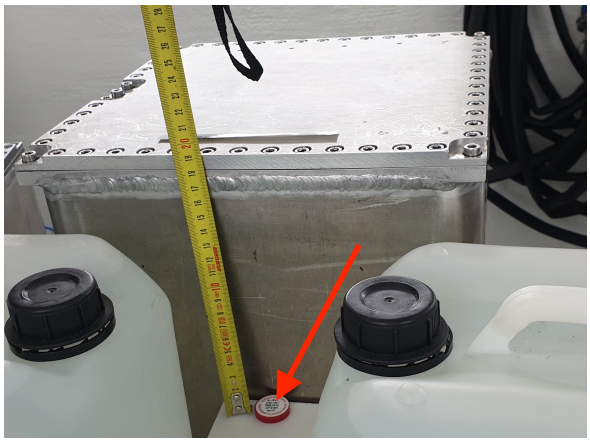

Figure 5.4: The placement of the ^{60}Co source, indicated by the red arrow

5.3 Study using a moderated neutron source

From the background measurement as well as the gamma-ray calibration the basic characteristics of the detector is known. To learn how the detector reacts to a moderated neutron source a setup using an AmBe source inside a moderator was performed.

The AmBe source, previously stored behind the aquarium at the STF, was used. The AmBe source was placed in a moderator, the same moderator as used in [25], and the moderator was placed in front of the detector, a little to the right of the center of the detector. The placement of the moderator and detector is shown in figure 5.5. The moderator used is a large block of polyethylene with a cylindrical hole where the source can be placed. All sides are made of aluminum covered with a thick layer of Gd_2O_3 paint. The front shielding side of the moderator was taken off the moderator to give the neutrons an unblocked path through the front, resulting in moderated neutrons flowing from the front. The moderator from the front can be seen in figure 5.6. The data acquisition was run for 45 minutes.

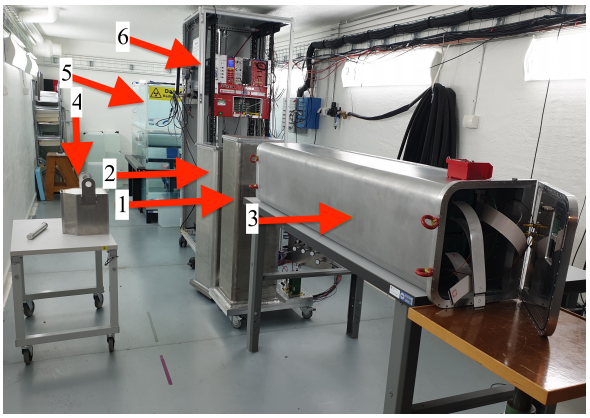

Figure 5.5: The setup of the Multi-Grid detectors and the moderator. The arrow numbered 4 indicates the moderator. The arrow numbered 1 indicates the CSPEC Multi-Grid detector, the arrow numbered 2 show the sequoia detector and the arrow numbered 3 points to the LET detector. The arrow numbered 5 indicates the aquarium of the STF, behind which the AmBe source is stored when it is not used. Lastly the arrow numbered 6 indicates the rack for the modules used for the CSPEC Multi-Grid detector.

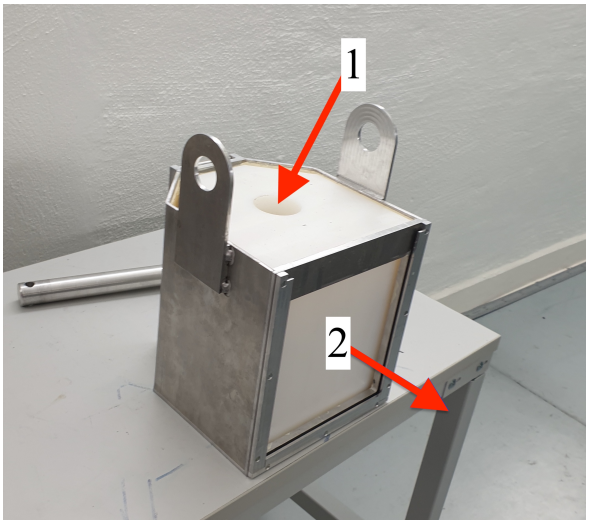

Figure 5.6: The moderator seen from the front. The arrow numbered 1 indicates where the fast neutron source is placed, while the arrow numbered 2 indicates in which direction the thermal neutrons exit the moderator.

5.4 Data processing

From one neutron interaction both one wire and at least one grid are expected to provide a signal. This is both expected from the detection principle, and necessary to determine the position of detection in the detector. Events including both one wire and between one or more grids are called coincidence events. The reason for the multiple grid option is described in chapter 3.

A signal from a wire or a grid has obtained a certain charge from the ionization process

of the gas atoms. The charge from the possibly multiple grids are added together and described as the grid charge, while the charge from the wire is described by the wire charge.

As described in chapter 3 the energy deposited by the α or Li particle, directly correlated to the resulting charge released, depends on how far into the $^{10}B_4C$ coating the neutron is captured. This means coincidence events corresponding to captured neutrons can be detected with low wire and grid charge. Gamma-rays are mostly expected to be attenuated by the aluminum vessel, however the interaction with the aluminum both in the vessel and in the grids of the detector is expected to result in free electrons. These will ionize the gas resulting in signals. The corresponding coincidence events are expected to have a low wire and grid charge.

For this reason, one way to discriminate against gamma-rays is to choose a software charge discrimination threshold, below which the coincidence events are not included. This means that the coincidence events with grid or wire charge below a chosen discrimination threshold are filtered out of the data. This threshold is set to 550 adc due to previous tests in previous Multi-Grid prototypes, and the coincidence events with grid charge above 550 adc as well as wire charge above 550 adc are called calibrated coincidence events. The coincidence events which have wire charge or grid charge below the discrimination threshold at 550 adc are described as being in the low charge region.

This discrimination threshold will also filter out neutron events. The idea is however that the signal to background ratio improves by discriminating against gamma-rays, not necessarily that all neutron events have to be detected.

6 Characterization of the Multi-Grid detector

In this chapter results from the measurements described in chapter 5 are presented. The count rate of coincidence events is calculated for all measurements and discussed. The detector characteristics and count rate in the measurements are studied.

The first three measurements were background measurements, two performed at Utgård and one at the STF. The fourth measurement was a gamma-ray threshold calibration. The fifth and last measurement was performed using a thermalized neutron source.

All measurement data are presented in the same manner as shown in figure 6.1. The data shown are from a 1 second measurement with a single coincidence event. This means only one voxel of the detector have triggered, i.e. one voxel has collected 100% of all coincidence events.

Figure 6.1 (a) shows a projection of the number of counts from the front of the detector as a function of wire row and grid number. Figure 6.1 (b) presents a projection from the right of the detector as a function of wire number and grid number. Figure 6.1 (c) shows a projection from the top of the detector as a function of wire row and wire number. Together figures 6.1 (a)-(c) indicate that the coincidence event occurred in row number 2, wire number 7 and grid number 25.

Count rate as a function of deposited charge in terms of adc units is shown in figure 6.1 (d) for wires (black) and grids (red). The measured charge in this event corresponds to 1500 adc and 2000 adc in grids and wires respectively. In figure 6.1 (d) the calibrated coincidence events are shown (both wire charge and grid charge above 550 adc) and since there is only one coincidence event which also fulfills the criteria for being called a calibrated coincidence event, no raw coincidence events are shown in figure 6.1 (d) (the raw coincidence events and the calibrated coincidence events are the same in this case).

A 2 dimensional plot of the count rate as a function of both charge collected by girds and by the wires is presented in figure 6.1 (e). The coincidence data point with wire charge equivalent to 2000 adc and grid charge 1500 adc is indicated with a black arrow.

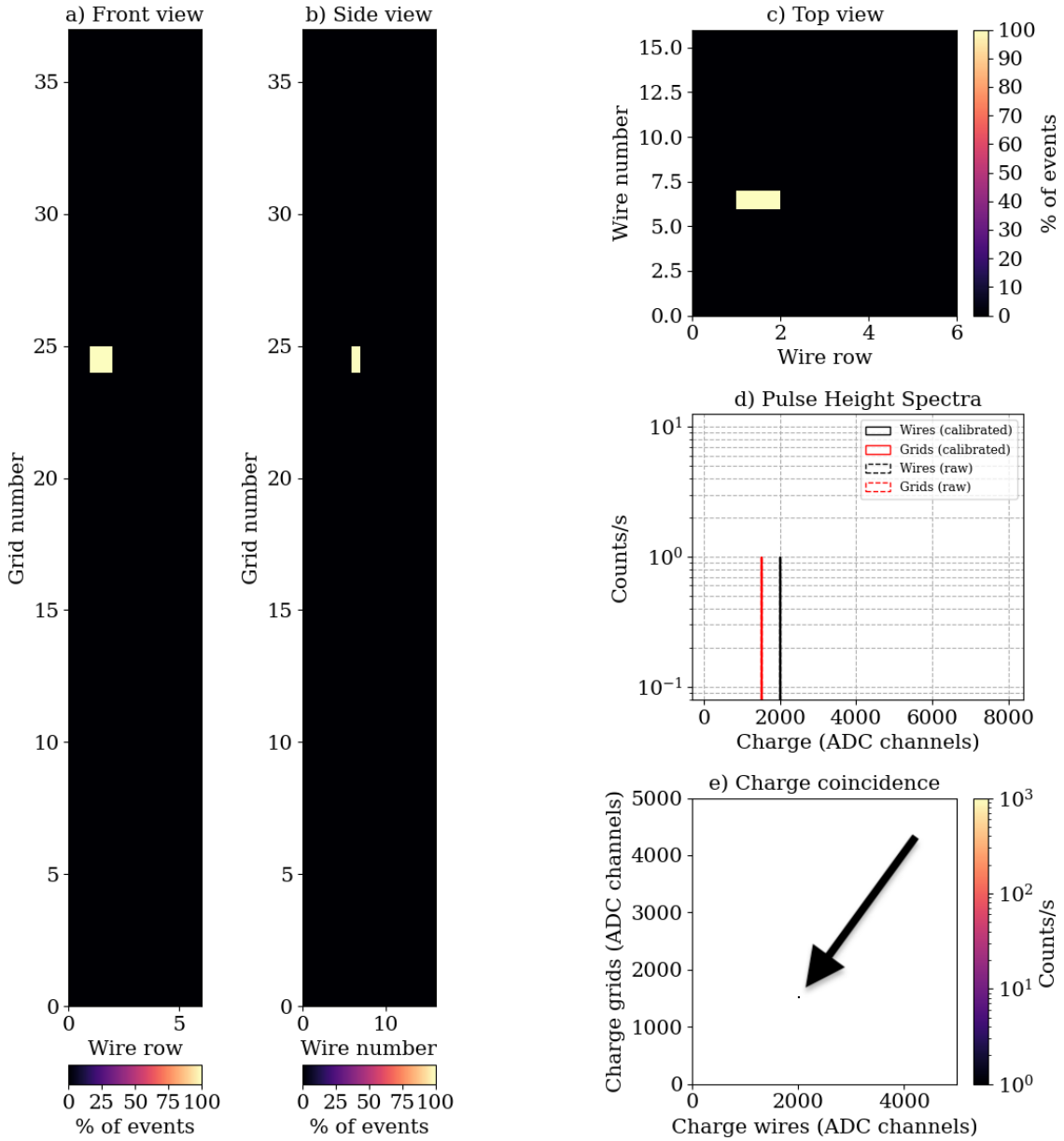

Figure 6.1: The result from a measurement with a single coincidence event during a one second measurement. This coincidence event includes a wire and a grid with a charge corresponding to 2000 adc and 1500 adc respectively. The plots are showing the same cross-sections as in figure 3.3. (a) the cross section as seen from the front of the detector, integrated over all the 16 wire numbers. (b) the cross section as seen from the right side of the detector, integrated over all 6 wire-rows, is plotted. (c) the cross section as seen from the top of the detector, integrated over all 37 grids. (d) the pulse height spectra of the measurement, both raw coincidence events and calibrated coincidence events, using a logarithmic scale for the Counts/s. Lastly in e) the charge coincidence between grids and wires for each cluster of data is shown. See text for more details.

6.1 Background studies

CSPEC is a quiet instrument by design. A special care was made in the shielding configuration to ensure an overall low neutron background. Any detector to be deployed in such an instrument must have a low intrinsic background count rate that does not compromise the performance of the instrument. To asses the detector intrinsic background several background measurements were taken. The first background measurement was performed at Utgård where the detector was placed on top of several Mirrobor™sheets and flushed with Ar/CO_2 (80/20 mix) gas for about a day, after which a measurement was started and run over 50 hours. This measurement was performed at Utgård which does not store any neutron sources. This means the number of detected neutrons is expected to be low, only detecting background neutrons, such as neutrons from secondary cosmic rays. For more details on the setup for this run, see chapter 5.

The resulting data is shown in figure 6.2. The number of calibrated coincidence events (with wire and grid charge above 550 adc) was 4.318 Hz, which is 47 % of all raw coincidence events. This means about half of all coincidence events have a wire and grid charge corresponding to above 550 adc.

The fact that there is recorded data, and that coincidence events could be reconstructed, indicates that the detector and its readout electronics where functioning.

In the front view in figure 6.2 (a) the highest count rate can be observed in the bottom left of the detector (grid number 1 to 15, wire rows 1-4). On the other hand, the top half of the detector has the lowest count rate (grid number 22 to 33, wire row 1 to 4) where the minimum region has about half of the count-rate compared to the maximum count-rate. In the side view in figure 6.2 (b) the highest count rate is at the front of the detector (wire row 1 to 3), especially towards the bottom of the detector (grid number 1). The count rate goes down from the front to a lower count rate towards the back of the detector. The lowest count rate of the detector is towards the back in the top half of the detector (grid number 21 to 36, wire number 5 to 16), except towards the very top where the count rate is higher (grid number 37). It is also discernible that wire number 9 has a lower count rate compared to the rest of the wire numbers. In the top view in figure 6.2 (c) the highest count rate is at the front of the detector (wire number 1) and decreasing towards the back. The left side also has a higher count rate compared to the right side of the detector. It can also be noted that at wire number 9, wire row 1 the count rate is exactly 0.

The higher count rate towards the bottom of the detector is due to the partial internal shielding of the detector. Only the top part of the detector has an internal Gd_2O_3 shielding on the inner sides of the vessel, as shown in figure 3.5 (b), as has been left from a previous experiment. This means that the top part of the detector is shielded from neutrons entering the right and the left side of the detector. The absorption of neutrons leads to gamma-ray emission. These, however, are expected to interact less inside the detector and result in low charge coincidences.

The higher count rate on the left side of the detector in figure 3.5 (c) can be explained by the geometry of the detector. The entire detector is not seen, the last two wire rows to the right are not used to take data as explained in chapter 3. This means the

lower count rate is actually towards the middle of the detector, not in the right of the detector. This is expected when measuring background since the particles detected travel from all directions, and since the particles are attenuated in the detector not as many particles reach the innermost part of the detector.

However, this correlation cannot be observed between the front and the back of the detector. This has to do with the radiation not necessarily entering the detector from all directions in the same quantity. Since the back of the detector is covered with Mirrobor™and the back of the grids are shielded with Gd_2O_3 neutrons have a low probability of entering the detector this way. The higher rate towards the front of the detector is thought to be background neutrons, for example neutrons from cosmic rays. Since only few neutrons enter from the back of the detector the lowest rate is expected in that reagion of the detector.

The lower count rate in wire number 9 in figure 6.2 b) and the wire with 0 count rate in figure 6.2 c) can be explained by a nonfunctioning wire. This might be due to some broken connection in the hardware of the detector, or that the wire was faulty.

In the pulse height spectra in figure 6.2 (d) a prompt peak is present before 550 adc (dashed line). This peak is therefore not a part of the calibrated coincidence events. After the prompt peak the distribution decreases exponentially until saturation is reached. The charge collected by the wires saturates is at 4096 adc, while the grids have a saturation peak at 4800 adc. Lastly the black curve (wires) is lower compared to the red curve (grids) close to the 550 adc cut off.

The wire curve (black) being lower compared to the grid curve (red) for the calibrated coincidence events in figure 6.2 (d) is due to the charge filter being applied for both grids and wires. Since several grids are usually in coincidence together with at least another grid the probability of some charge leaking into a neighboring grid is not negligible. This leaked charge can be under 100 adc units, not reaching the 100 adc hardware threshold, resulting in this grid charge being lost for the event. This means the grid charge can be under 550 adc, while the wire charge is still above 550 adc. This will only happen close to the 550 adc cutoff since the hardware threshold is 100 adc, meaning if there is a charge leaking into two grids the maximum charge leakage lost is 200 adc. This is also what is seen, the filtered wire curve is only lower than the grid curve for about 50 adc which is well below the possible 200 adc.

In the charge coincidence plot in figure 6.2 (e) the charge between the grids and the wires is close to linear. The wire charge has a sharp cut of at 4096 due to charge saturation.

The saturation peak at 4096 adc is the maximum dynamic range or the mesytec MMR cards. The grids do not exhibit the same saturation feature since a pulse can be divided onto several grid channels. The wider grid peak at 4800 adc is the grids saturation peak. This comes from a coincidence event with more than one grid, where one of the grids is assigned the highest possible charge 4096 adc, and the remaining grids gets assigned around 700 adc. This creates a much wider peak since the remaining grids can have different charges, while since only one wire is allowed to give a signal at a time the overflow peak is sharp for the wires.

This is also the reason behind the sharp cut of in the charge coincidence plot. Since only one wire is allowed to give a signal, the maximum charge achievable in adc from the wires is 4096 adc for one coincidence event. Since several grids can give a signal simultaneously this cut of is not present in the grids. The linear relation between grid charge and wire charge means that the wire collects as much charge as the grids and vice versa. This indicates that the coincidence event is due to a released charged particle in the gas, and not some other unexpected event.

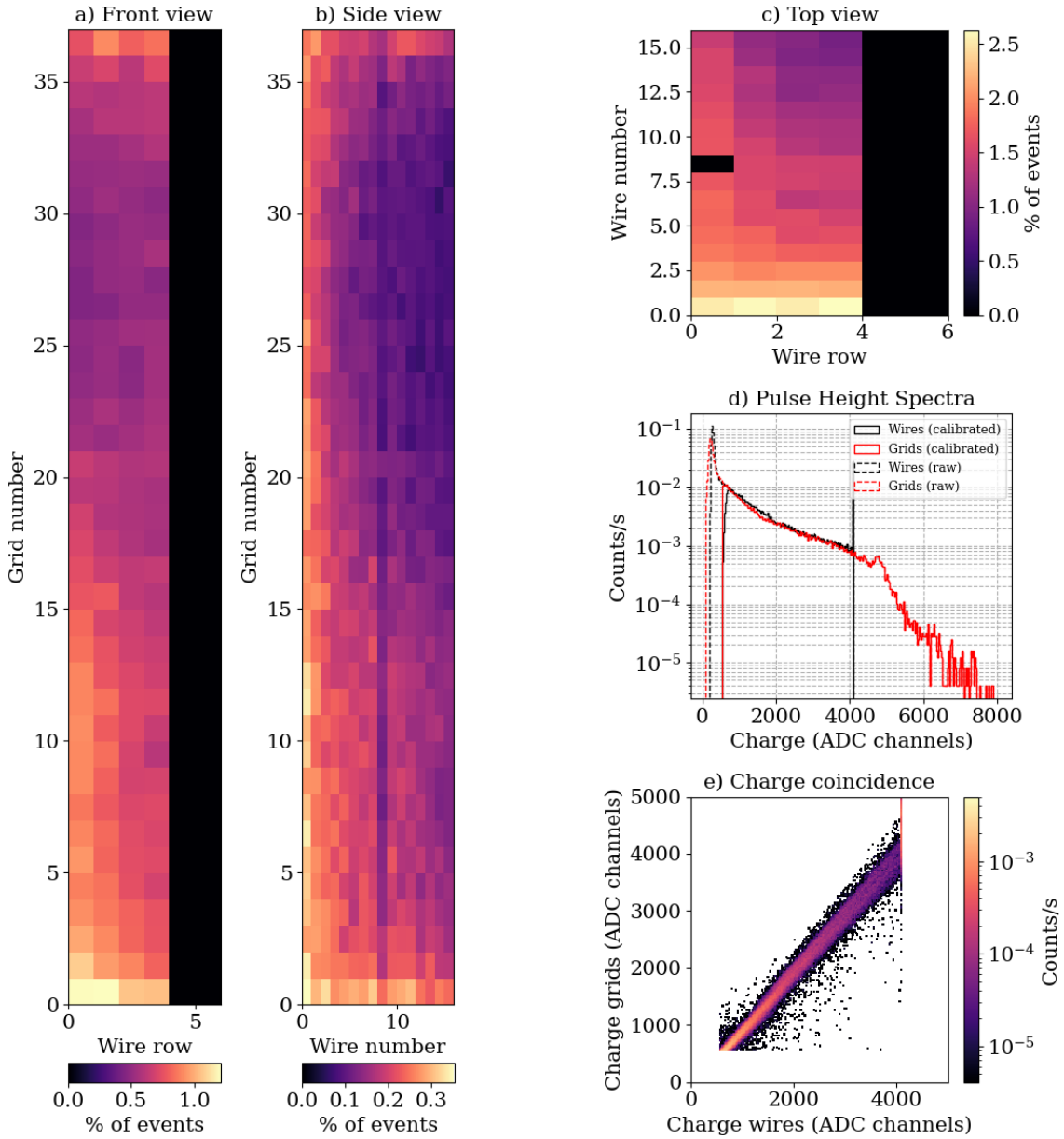

Figure 6.2: The data from the background measurement at Utgård showing the calibrated coincidence events (both wire charge and grid charge above 550 adc). (a) shows the count rate in each cell as a projection from the front of the detector, (b) projection from the right side of the detector, (c) projection from the top of the detector.(d) shows the pulse height spectra. The amount of raw coincidence events was 9.163 Hz, of those were 4.318 Hz from calibrated coincidence events (with both grid and wire charge above 550 adc). This means that the calibrated coincidence event rate was 47% of the raw coincidence event rate. (e) shows the charge coincidence for each cluster of data. For more details on the plots see figure 6.1.

For the second background measurement the vessel was covered on all sides with Mirrobor™shielding. Background measurement data taken over 70 hours is presented in figure 6.3. Neutrons in the thermal range are now expected to be shielded out, resulting in a lower number of coincidence events detected compared to the setup

without the Mirrobor™shielding.

The calibrated coincidence event rate was 0.472 Hz which accounts for 14% of the raw coincidence events. This means a larger fraction of the of the raw coincidence is in the low charge range (wire charge or grid charge below 550 adc) compared to the previous background measurement. Since neutrons in the thermal regime are expected to be shielded out of the detector, other detected particles such as gamma-rays are expected to be more dominant than in the setup without the external shielding. The count rate in the low charge range is also lower in this measurement, indicating neutrons in the thermal range are being detected in the low charge regime, which is expected.

In figure 6.3 (a) the count rate is uniform for the entire detector except that in the bottom grid (grid number 1) of the detector has a higher count rate compared to the rest of the detector, about a factor of 5 higher. In figure 6.3 (b) the count rate is again uniform, except for a higher count rate in the bottom grid of the detector, again about a factor of 5 difference. In figure 6.3 (c) the back wires of the detector has the highest count rate compared to the rest of the detector, about a factor of 1.3 to 2 higher.

The higher count rate towards the bottom of the detector might be due to a gap in the shielding towards this end of the detector. It might also be that something towards the end grid (like the soldering) contains traces of natural α emitters. The higher count rate towards the back of the detector might be due to a component radiating (for example the aluminum grid back pieces might contain α emitting radioactive components). Another possibility is that the ground together with the concrete flooring at Utgård are moderating fast neutrons from cosmic rays, resulting in thermalized neutrons radiating from the ground. However, as it only seems to be the back layer, wire number 16, that has the higher count rate it is unlikely that it is due to thermalized neutrons, since neutrons are attenuated through the detector.

The pattern seen in the background measurement without Mirrobor™shielding is not present in the measurement with external shielding. This suggests that the higher count rate towards the front of the detector in the previous measurement is due to neutron attenuation throughout the detector and the lower count rate towards the back top of the detector are due to fewer neutrons reaching this part of the detector.

In figure 6.3 (d) the pulse height spectra of the measurement is shown. It has a prominent initial peak higher compared to the previous measurement.

From the pulse height spectra of both measurements performed at Utgård it is noticeable that the peak in the low charge region is more pronounced in the shielded data compared to the unshielded data. This can also be gathered from the fact that the calibrated coincidence events represent only 14% of the raw coincidence events compared to the 47% in the previous measurement. If the gamma-ray discrimination threshold is set correctly, this would mean that a larger fraction of all recorded coincidence events is due to detected gamma-rays in the shielded setup, compared to the unshielded setup.

In figure 6.3 (e) the charge collected by grids and wires in coincidence are shown. This plot shows a linear shape until the wire charge goes up to 4096 adc, after which there

are no hits. The grid charge does not have this cutoff.

It is noticeably less counts for the shielded measurement compared to the measurement without the Mirrobor™shielding, however apart from that they are similar in appearance.

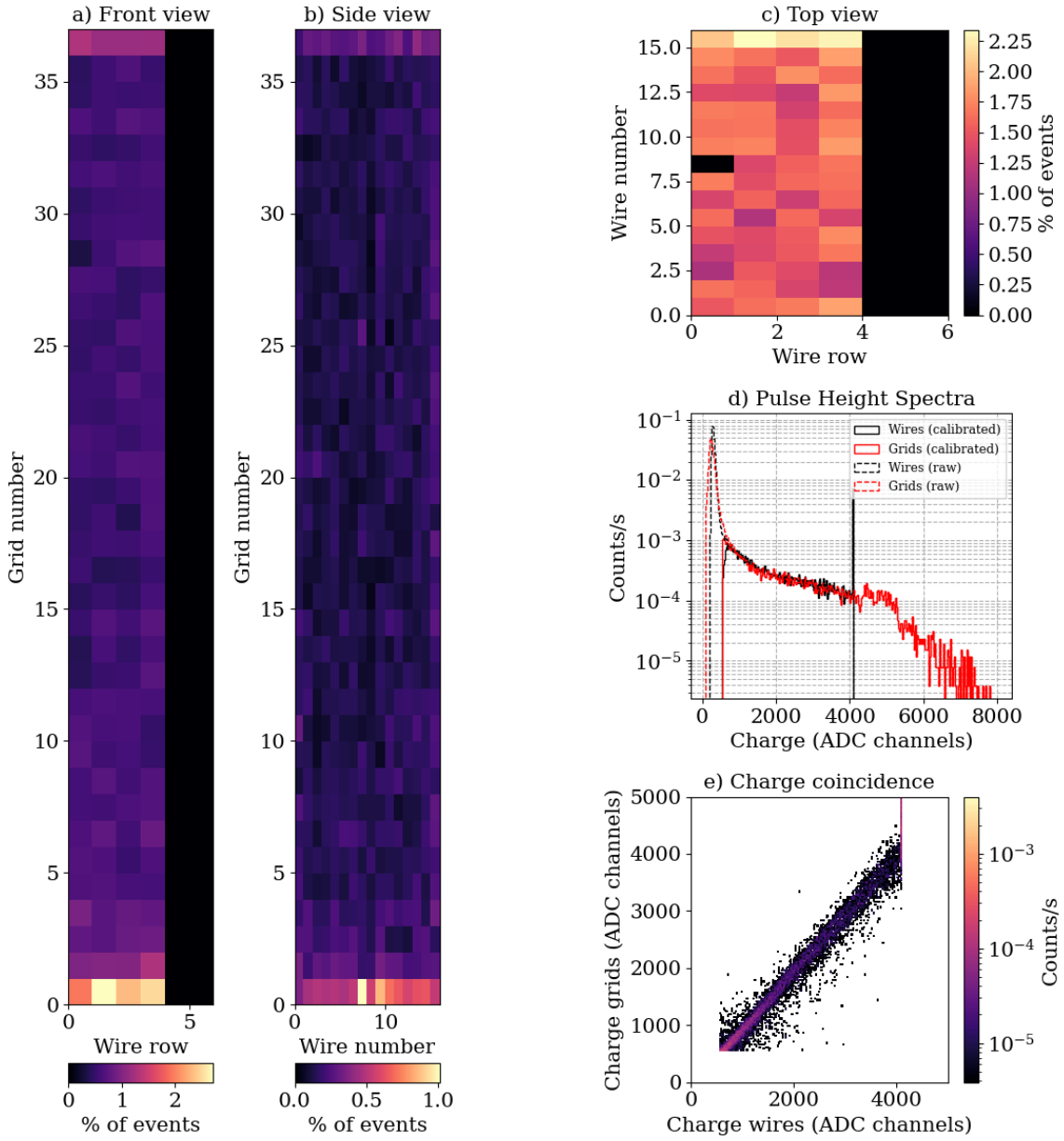

Figure 6.3: Calibrated coincidence events (grid charge and wire charge above 550 adc) from the background measurement using the shielded vessel setup at Utgård. (a) shows the count rate in each cell as a projection from the front of the detector, (b) projection from the right side of the detector, (c) projection from the top of the detector. (d) shows the pulse height spectra. The raw coincidence event rate was 3.432 Hz and the calibrated coincidence event rate was 0.472 Hz, or 14% of the raw coincidence event rate. (e) shows the charge coincidence for each cluster of data. For more details on the plots see figure 6.1.

After the two background measurements were performed at Utgård the detector was moved to the STF for further testing. The first test performed at the STF was a background measurement to see how the detector reacted in a more radioactive area. The detector was placed on the floor of the STF and was flushed with gas for 24 hours before being connected. The measurement was then taken over 15 hours, for the details on the setup see chapter 5. Due to neutron sources present at the STF the number of coincidence events per second is expected to be higher, compared to the background measurements performed at Utgård.

Data from the background measurement performed at the STF are presented in figure 6.4. The calibrated coincidence event rate was 243.1 Hz which is about 50 times higher compared to the measurement performed with the unshielded setup at Utgård. This might be as a result of the presence of a PuBe source in the water tank and the AmBe source behind the water tank at the STF. The higher rate might also be due to different gamma-ray sources present at the STF. The calibrated coincidence events are now 81% of the raw coincidence events which is higher compared to both measurements performed at Utgård. Since the calibrated coincidence events are expected to be neutron events, this might mean a larger portion of the raw coincidence events are neutrons in the thermal range. The STF has a higher amount of other particles, such as fast neutrons and energetic gamma-rays which might be detected as calibrated coincidence events (grid charge and wire charge above 550 adc).

In figure 6.4 (a) the highest count rate is found at the bottom left of the detector (grid number 1 to 16, wire row 1 to 4). On the other hand the top half of the detector has the lowest count rate (grid number 21 to 35) by a factor of 2. The very top of the detector (grid number 36 to 37) has a higher count rate compared to the rest of the top half of the detector, about a factor of 2 higher. In figure 6.4 (b) the highest count rate is found at the front of the detector (wire number 1), especially towards the bottom of the detector (grid number 2 to 17). The count rate goes down from the front to a lower count rate towards the back. The lowest count rate of the detector is towards the back-top half of the detector (grid number 18 to 35, wire number 5 to 16), the count rate is a factor of 4 lower here compared to the region with the maximum count rate. Towards the very top of the detector the count rate is higher (grid number 37) compared to the region with the minimum count rate, a factor of 2 higher. In figure 6.4 (c) the highest count rate is at the front of the detector (wire number 1 to 3). The lowest count rate is towards the right back of the detector (wire row 3 to 4, wire number 10 to 16), a factor of 3 lower compared to the maximum.

This measurement shows similar characteristics as the background measurements performed at Utgård. However, in this measurement the higher count rate at the bottom could also be explained by the fact that the detector is now standing up, and since Ar, the active gas in the detector, is heavier than air it will fill the bottom of the detector first. Meaning that if there is a gas leak, resulting in the detector not being filled by gas, the count rate would go down at the top of the detector. However, since the rate still goes up towards the upmost top of the detector this explanation is not as likely.

In figure 6.4 (d) the pulse height spectra of the measurement is shown. It reaches the maximum at about 550 adc and the decreases until the wires saturates at 4096 adc, after which the grids have a broader saturation peak at about 4800 adc.

The pulse height spectrum no longer has the initial peak at the low charge region observed at Utgård. Instead the distribution exponentially decreases after the maximum. This would suggest smaller portion of the detected coincidence events are gamma-ray induced events.

In figure 6.4 (e) the charge collected by grids and wires in coincidence are shown. This plot shows a linear shape until the wire charge goes up to 4096 adc, after which there are no hits. The charge on the grids do not have this cutoff. This looks similar to the shape seen in previous measurements.

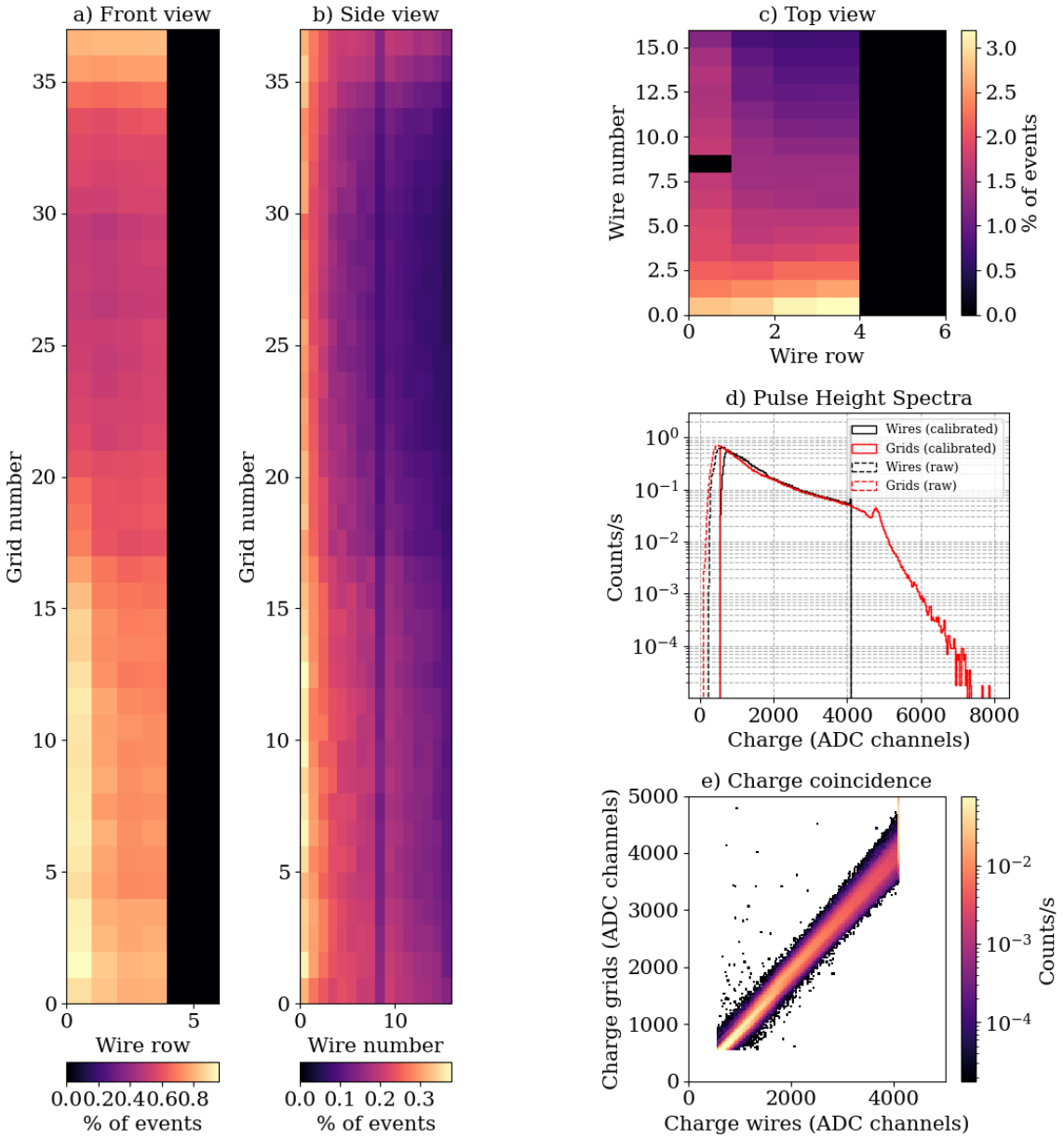

Figure 6.4: The calibrated coincidence events from the background measurement performed at the STF. (a) shows the count rate in each cell as a projection from the front of the detector, (b) projection from the right side of the detector, (c) projection from the top of the detector. (d) shows the pulse height spectra. The raw coincidence event rate was 298.6 Hz while the calibrated coincidence event rate was 243.1 Hz, or 81% of the raw coincidence event rate. (e) shows the charge coincidence for each cluster of data. For more details on the plots see figure 6.1.

6.2 Gamma-ray threshold calibration

The detector is known to be sensitive to gamma-rays. In a previous prototype of the Multi-Grid detector gamma-rays were found to be detected as coincidence events with

the grid charge and wire charge correlating to below 550 adc. This has been used as a discrimination threshold in the software stage to discriminated against gamma-ray coincidence events.To evaluate this discrimination threshold for gamma-rays, a threshold calibration was performed. A ^{60}Co source was placed directly in front of the detector, fixed for the 10 minuet run. For more details on the setup see chapter 5.

The calibrated coincidence events from this measurement is presented in figure 6.5. This means the data is not expected to contain gamma-ray coincidence events. The total amount of raw coincidence events was 877.5 Hz, of which 216.4 Hz are calibrated coincidence events. This means that the coincidence events in the low charge regime are about 76% of the total count rate, compared to 19% in the background measurement performed at the STF. Since the amount of calibrated coincidence events (216.4 Hz) is in the same ballpark as in the background measurements calibrated coincidence events (243.1 Hz) this indicates that the low charge coincidence events (below 550 adc) do come from the gamma-ray source. The gamma-ray source was the only added part to this measurement compared to the background measurement. The calibrated coincidence event rate not being exactly the same might be due to the non negligible statistical variation in the short measurement time with the gamma-ray source.

In the front view in figure 6.5 (a) the highest count rate is located at the bottom left of the detector (grid number 1 to 16, wire row 1 to 4). The top half of the detector has the lowest count rate (grid number 20 to 35, wire row 1 to 4), about half compared to the highest count rate region, except the top grids (grid 36 to 37) which have a higher count rate than the rest of the top half of the detector. From the side view in figure 6.5 (b) the highest count rate is towards the bottom front of the detector (grid number 1 to 20, wire number 1 to 4) The rate decreases from the front of the detector to the back of the detector. The lowest count rate is located at the top half back of the detector (grid number 18 to 35, wire number 6 to 16), the rate is about a fourth here compared to the high count region.The top grids (grid number 36 to 37) have a higher count rate compared to the rest of the top half of the detector, about 2 times higher. Wire number 9 have a lower count rate compared to the wire numbers around it. From the top view in figure 6.5 (c) the highest count rate is towards the front of the detector (wire number 1 to 3). The count rate decreases to a minimum at the back of the detector, wire number 12 to 16 in wire row 2 to 4 is especially low, about 3 times lower compared to the high-count region. Wire number 9 at wire row 1 has a count rate of 0.

The characteristics seen in figure 6.5 are very similar to those seen in figure 6.4, which shows the background measurement at the STF. This indicates the gamma-ray source added to the setup of this measurement has little to no contribution to the characteristics. This either means gamma-rays are detected evenly in the detector, few to non are detected, or that the gamma-ray coincidence events are being discriminated against by the applied threshold.

The pulse height spectra in figure 6.5 (d) starts with a sharp peak which ends at around 550 adc. The sharp peak is about a factor of 50 higher compared to the rest of the spectra.

This sharp peak at low charge channels not seen at STF before, is more similar in

shape to the background measurement performed at Utgård with the detector covered with Mirrobor™sheets. In both measurements the initial peak is about a factor of 50 higher compared to the surrounding spectra. This indicates it might be gamma-rays detected in the shielded background run at Utgård. The charge coincidence plot in figure 6.5 (e) shows what charge interval is studied. The relationship between the charge collected by the grids and wires is linear.

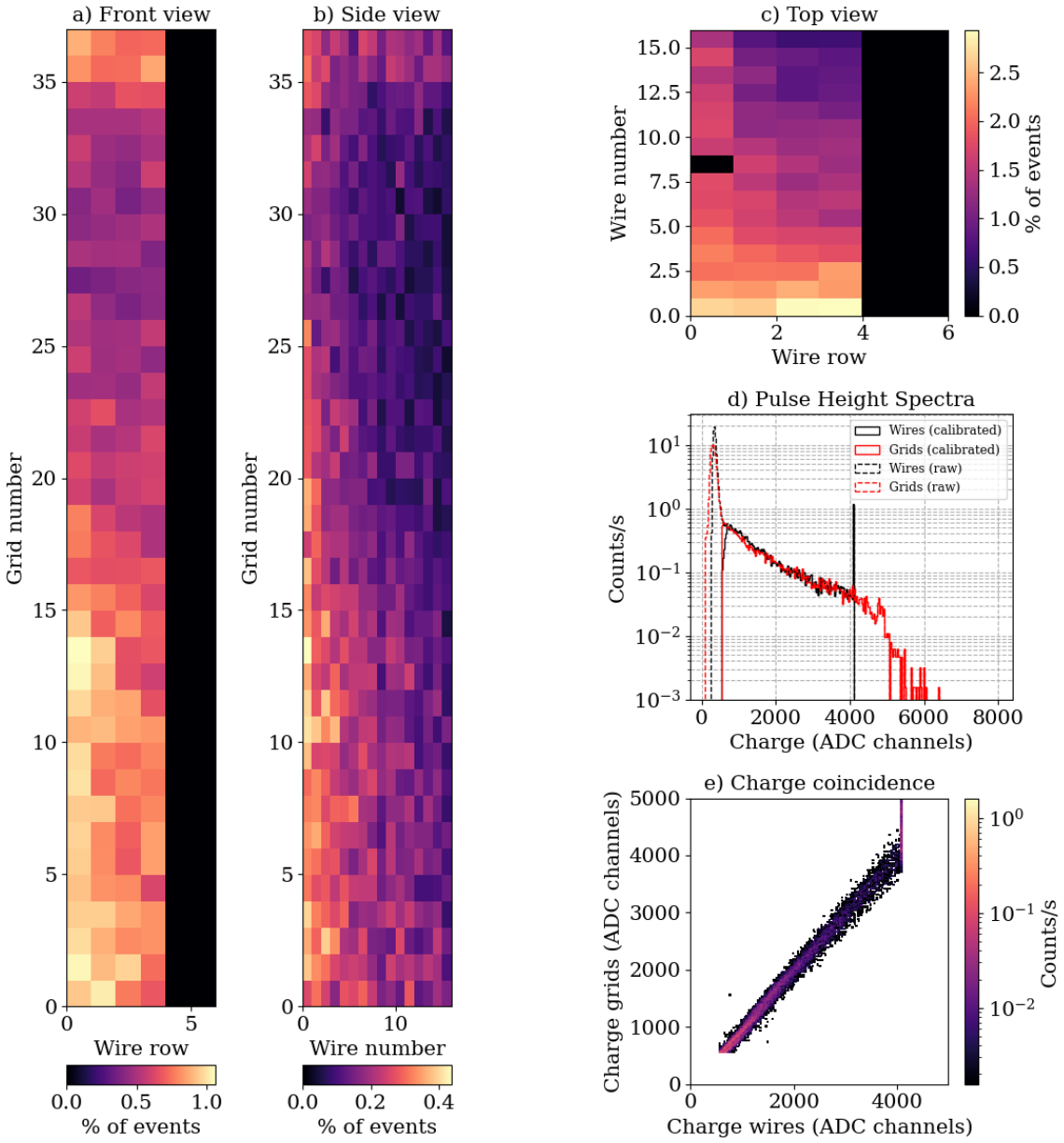

Figure 6.5: The calibrated coincidence events from the measurement performed at the STF using a ^{60}Co source .(a) shows the count rate in each cell as a projection from the front of the detector, (b) projection from the right side of the detector, (c) projection from the top of the detector. (d) shows the pulse height spectra. The raw coincidence event rate for the entire detector was 877.5 Hz of which 216.4 Hz, or 24 %, was from the calibrated coincidence events. (e) shows the charge coincidence for each cluster of data. For more details on the plots see figure 6.1.

To see if gamma-rays from ^{60}Co leave any trace in the detector the raw charge coincidence events were also studied. This is presented in figure 6.6.

In figure 6.6 a clear, not seen before, irregular pattern is visible in the front view, the side view and in the top view. From the front view in figure 6.6 (a) a higher count rate is present in grid numbers 26, 21,19 and 31 as well as in wire row 2 and wire row 4. The bottom half of the detector has the lowest count rate, going down to 0. From the side view in figure 6.6 (b) the highest count rate is towards the front of the detector. Grid numbers 19, 21, 26 and 31 are especially high. The bottom half of the detector has the lowest count rate, again going all the way down to 0. From the top view in figure 6.6 (c) the highest count rate is towards the front of the detector. Wire rows 2 and 4 have higher count rates.

Compared to figure 6.4 which is the background measurement performed at the STF something completely different is seen. The gamma source is placed 19 cm from the top of the detector which corresponds to about grid number 31 or 32. One of the higher count rates is found in grid number 31, however the absolute maximum is located in grid number 26. Since some gamma rays will have interacted with the aluminum, resulting in free electrons and altered paths of the gamma-rays, the pattern from the ^{60}Co source is hard to predict. What is clear however is that the gamma-rays are detected in the top half of the detector, and that the strange pattern due to the gamma-rays, which is not seen in the calibrated coincidence events.

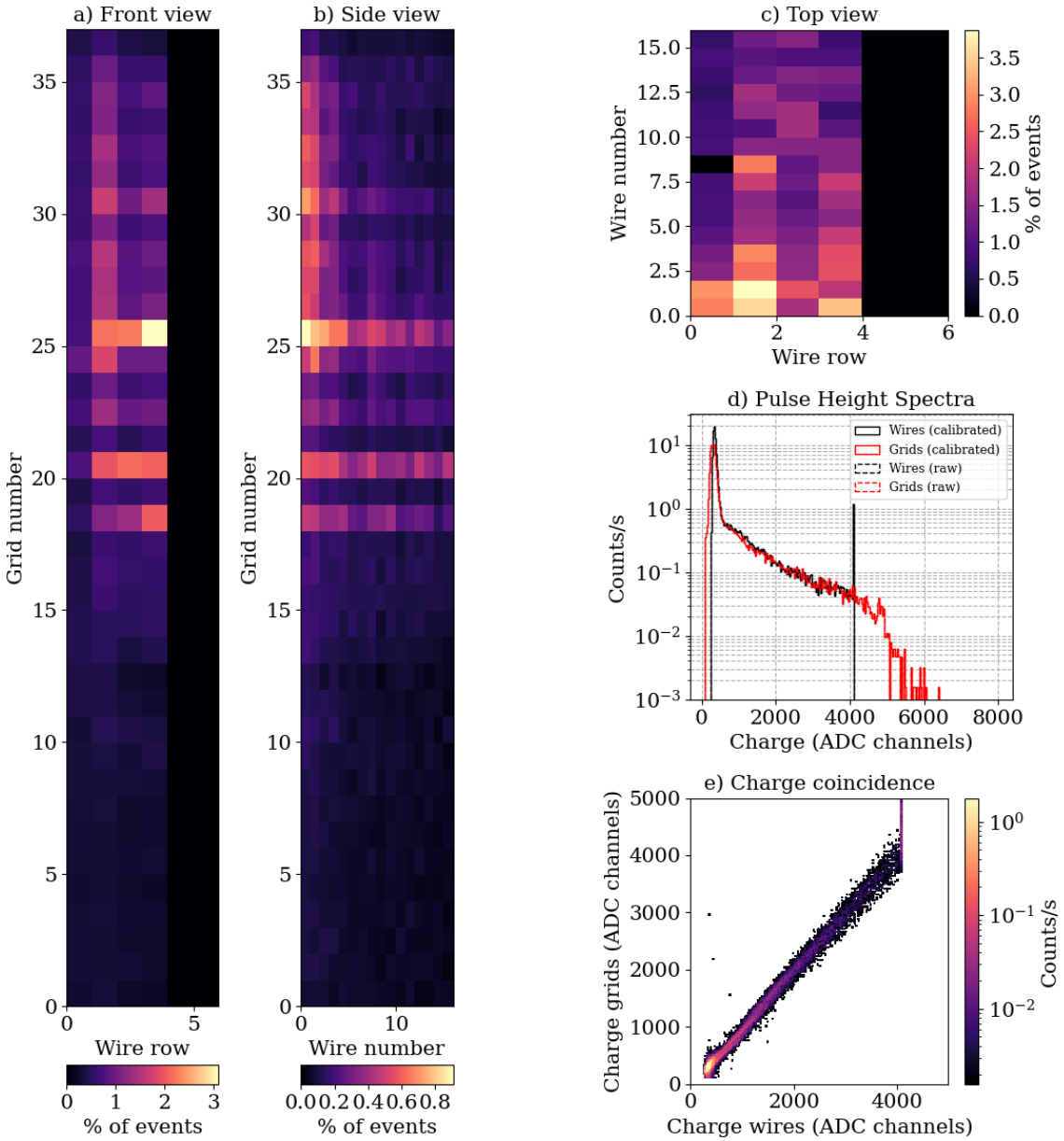

Figure 6.6: The raw coincidence events from the measurement using the ^{60}Co source.(a) shows the count rate in each cell as a projection from the front of the detector, (b) projection from the right side of the detector, (c) projection from the top of the detector. (d) shows the pulse height spectra. The raw coincidence event rate was 877.5 Hz. (e) shows the charge coincidence for each cluster of data. For more details on the plots see figure 6.1.

To further compare the measurement taken with the gamma-ray source and the background measurement the obtained pulse height spectra were subtracted. This is shown in figure 6.7. The clear difference is in the low charge regime (below 550 adc) where the initial peak is a factor of 100 larger compared to the region after the peak. This again indicates that the difference between the pulse height spectra with and without the ^{60}Co source, found in the low charge regime is most likely due to detected gamma-rays. This also indicates that the gamma-ray discrimination threshold set at 550 adc should be kept at 550 adc.

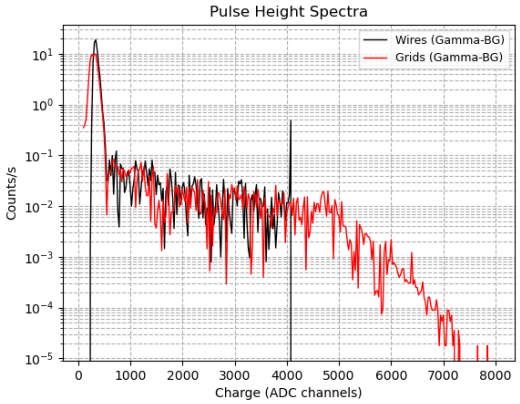

Figure 6.7: The pulse height spectrum from the gamma-ray minus the pulse height spectrum from the background measurement at the STF.

The results obtained from the gamma-ray source measurement at the STF was an indication that the 550 adc discrimination threshold set is well chosen to discriminate against detected gamma-rays. It is clear that some neutron events will also be filtered out due to this threshold, however the most important part is to reduce non-neutron events, not necessarily to detect all neutrons.

The 550 adc threshold could be studied in more detail by testing with different gamma-ray sources other than the ^{60}Co to cover a wider range of gamma-ray energies. At present this 550 adc threshold is used for both grids and wires, although this might not be optimum. The impact of choosing different threshold values for the grids and wires could be studied in detail, alternately to only set a threshold for the wires. Since an event usually includes several grids, the probability of some charge leaking to neighboring grids without reaching over the hardware threshold is not negligible. This may result in the grid charge being below the threshold, while the wire charge is above the threshold. These coincidence events would not be rejected if the threshold was only set for the wires.

6.3 Study using a moderated neutron source

To finally assess the detector response to thermalized neutrons, an AmBe source was put inside a moderator and placed at the front of the detector. This measurement was taken over 45 minuets. For more details on the setup see chapter 5. The calibrated coincidence events from the measurement is shown in figure 6.8. The calibrated coincidence event rate was 5332 Hz, or 77% of the raw coincidence event rate. The calibrated coincidence event rate is about 25 times higher compared to the calibrated coincidence event rate in the background measurement at the STF. However, the fraction of calibrated coincidence events to raw coincidence events are lower compared to the background measurement at the STF. This might be due to the AmBe source being a gamma-ray source as well as a neutron source, meaning more gamma-rays are being detected.

From the front view in figure 6.8 (a) the highest count rate is located towards the lower right of the detector. The lowest count rate is towards the top left of the detector (grid number 26 to 35, wire row 1 to 2). The count rate goes up at the top grids of the detector compared to the rest of the top half of the detector. In the side view in figure 6.8 (b) the highest count rate is towards the front of the detector. The count rate decreases to a minimum at the back of the detector. The lowest count rate is located in the top half back of the detector. In the top view in figure 6.8 (c) the highest count rate is located in the front right of the active detector. The count rate decreases to a minimum at the back of the detector.

The higher count rate towards the right of the active detector can be explained by the location of the source. This could also explain the lower count rate towards the top left of the detector. The higher count rate at the front of the detector compared to the back is expected since the source is placed at the front of the detector so moderated neutrons get attenuated traveling through the detector. The lower count rate towards the top back of the detector is not as prominent here as that in the background run at the STF. This indicates that the lower count rate in the background measurement was due to the shielding inside the detector. Since this will not shield the detector from thermal neutrons incoming from the front the internal shielding should not make much difference when a source is present.

However, the least count rate is still found in the top back of the detector. This can be a result from the side internal shielding reducing the amount of back scattering of thermal neutrons from the aluminum vessel into the detector. This effect will not be as prominent towards the top of the detector since only the right and left side of the top half of the detector has internal shielding, not the top lid of the detector, so the end grids might be hit by scattering from the top lid.

The pulse height spectra in figure 6.8 (d) shows a maximum at about 500 adc, and then a decrease until the charge of the wires saturate at 4096 adc. The grids have a broader peak at 4800 adc.

The pulse height spectra is similar to the pulse height spectra of the background setup at the STF.

Lastly in figure 6.8 (e) the charge coincidence between the grids and the wires are shown. This plot shows a linear shape until the wire charge goes up to 4096 adc. In this measurement there are some hits with a higher grid charge than in the corresponding wire.

Events with higher charge on the grids than wires might be double wire events, where one wire is triggered in the active part of the detector and one wire in wire rows 5 or 6. Since wire rows 5 and 6 were not readout, the fact that it is a double wire event is missed and they will thus be counted as coincidence events. Important to note is that such events with higher grid charge are very few compared to the main linear charge relation between grids and wires.

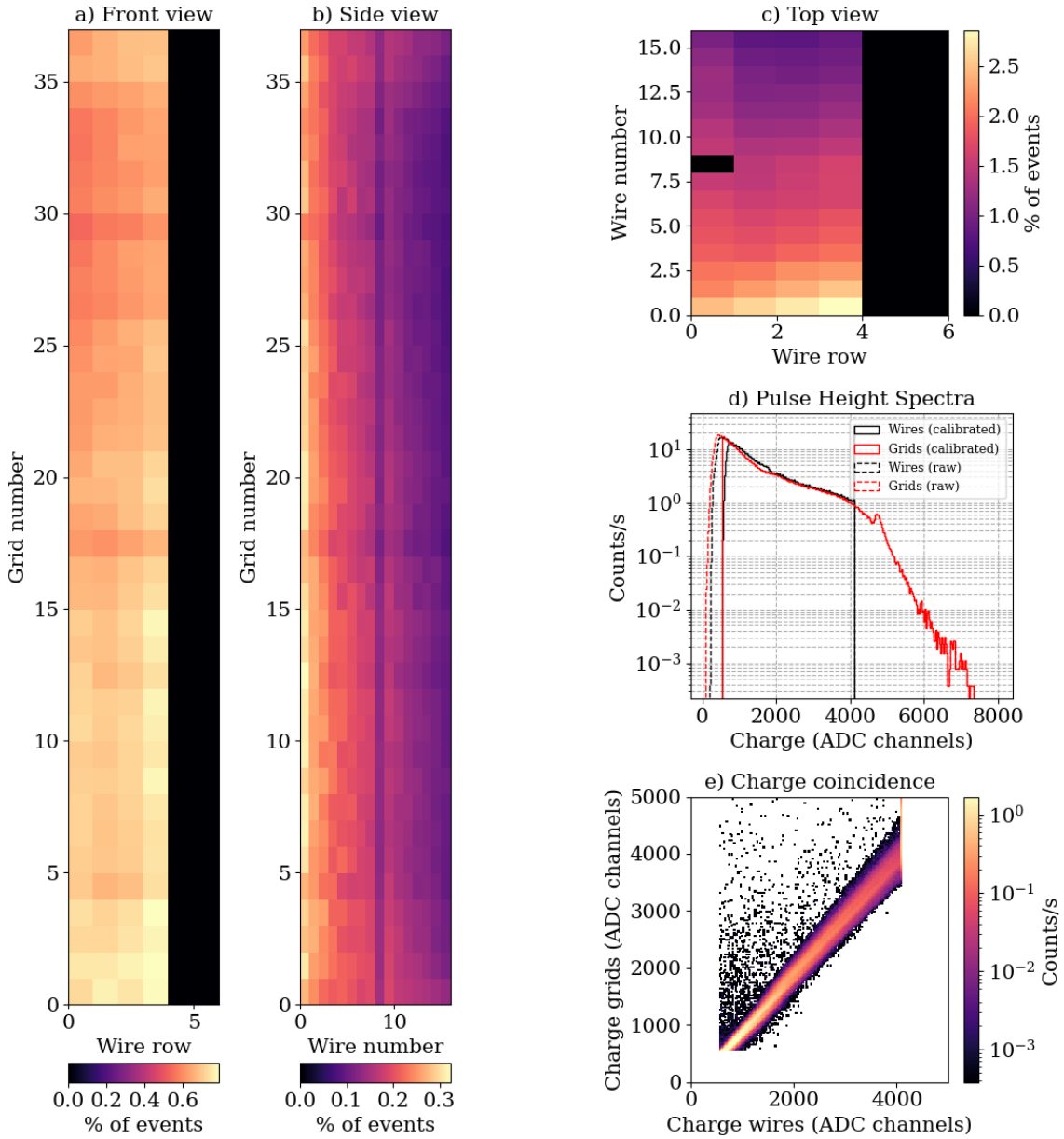

Figure 6.8: The calibrated coincidence events from the measurement using an AmBe source inside a moderator. (a) shows the count rate in each cell as a projection from the front of the detector, (b) projection from the right side of the detector, (c) projection from the top of the detector. (d) shows the pulse height spectra. The raw coincidence event rate was 6891 Hz, of which 5332 Hz were calibrated coincidence events, meaning the calibrated coincidence events were 77% of the raw coincidence events. (e) shows the charge coincidence for each cluster of data. For more details on the plots see figure 6.1.

To conclude, when a moderated AmBe source is introduced the calibrated coincidence events increase by a factor of 25, and the previously observed characteristic of the large dip in count rate towards the top back of the detector mostly disappears. This is only explained if it is neutrons that is being recorded by the detector. The gamma-ray discrimination threshold at 550 adc rejects about 20 % of the raw coincidence events, this can be explained by that the gamma-rays from the AmBe source is detected in

this region, as well as the presence of some detected thermalized neutron in this region.

The tests indicate that the CSPEC Multi-Grid detector does detect thermal neutrons. How effectively it detects them and how well it disregards non-neutron event, such as gamma-rays, are not studied in detail in this work. A preliminary gamma-ray discrimination threshold is set to 550 adc based on the results from the gamma-ray threshold calibration measurement. None of the tests performed have been quantitative, meaning none of the numbers can be directly compared to theory.

More quantitative studies, such as signal to background ratio and line-shape compared to 3He detectors, will be performed once the detector is shipped and tested at ISIS.

7 Commissioning the novel Multi-Grid detector at ISIS

In this chapter the measurements preformed at ISIS, as well as some preliminary results from these measurements are presented.

7.1 ISIS Neutron and Muon Source

ISIS is a muon and neutron source based at Rutherford Appleton Laboratory in Oxfordshire, UK. The muon and neutron beams are used to study structures at the atomic level. All muon and neutron instruments are free to use provided that all results are published in the public domain.

The ISIS facility starts with a high energy proton accelerator. It starts with the ISIS ion source which creates negatively charged hydrogen ions. These are then accelerated and focused through a Radio Frequency Quadrupole accelerator. Then further accelerated through a linear accelerator to 37% of the speed of light. Next the hydrogen ions are stripped of their electrons by a thin foil, leaving protons, which are further accelerated to 84% of the speed of light in a synchrotron. By the electric field the protons are also divided into 2 bunches over 10 thousand revolutions in the synchrotron. The proton bunch leaves the synchrotron to one of two target station. In target station one the proton bunch first hits a thin carbon target resulting in muons. The proton bunch then continues on to hit the tungsten target resulting in neutrons through spallation. In the second target station the proton bunch hits a main target directly and creates neutrons through spallation. The second target station is optimized for low energy neutrons [26].

Neutrons from the target are then guided in neutron beam lines and moderated to a suitable energy for the instrument they are to be used in. The LET instrument is a cold neutron multi-chopper spectrometer used for analyzing dynamics in condensed matter to gain understanding in the origin of material properties on a microscopic level. It uses inelastic scattering and studies the energy difference of a neutron before and after interacting with the condensed material. This energy difference is obtained with time-of-flight measurement of the neutrons from the time they leave the accelerator until they hit the 4 m long position resolved ^{3}He detectors used in the instrument [27]. The detectors are placed in the LET detector tank, shown in figure 7.1.

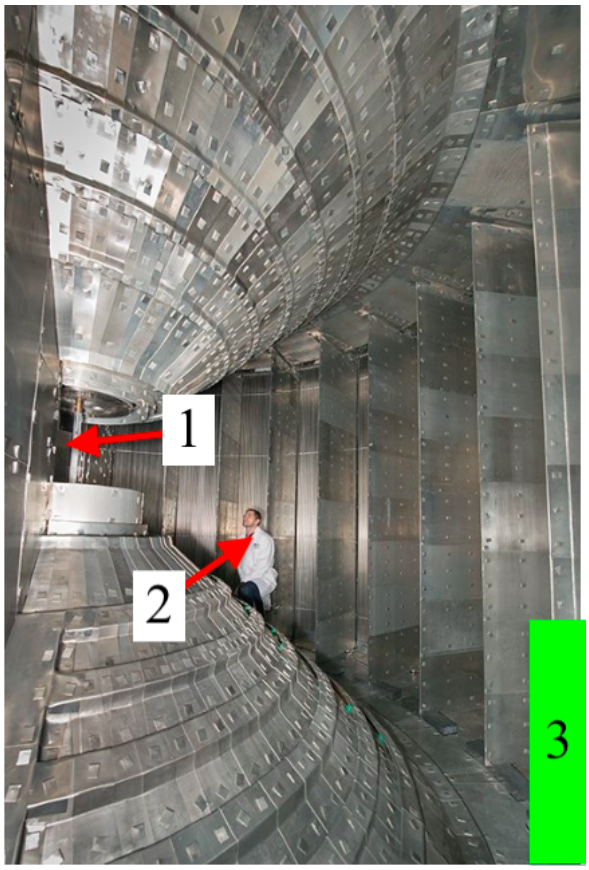

Figure 7.1: The LET detector tank. The red arrow numbered 1 points to the sample area, the red arrow numbered 2 indicates a person, behind which the ^{3}He detectors are placed. The green area numbered 3 indicates approximately where the CSPEC Multi-Grid detector was placed.

7.2 The CSPEC Multi-Grid detector at ISIS

To be able to evaluate the performance of the CSPEC Multi-Grid detector it has to be tested alongside already existing detectors in an instrument similar to the instrument it is intended to be used in, the CSPEC instrument. For that reason, the CSPEC Multi-Grid detector was shipped to ISIS to be tested alongside the ^{3}He detectors at the LET instrument. Before shipping the detector the internal shielding was properly installed so that the entire inside of the detector vessel walls was covered with Gd_2O_3 shielding, as seen in figure 3.5 (a).

At LET performance parameters, such as signal to background ratio and line-shape have been evaluated. The actual beamtime for the test was 2 days, however the detector was at ISIS 2 weeks before in order to be ready to measure as soon as the beam became available.

The detector was sent to ISIS by truck. To make sure no wires were broken the detector was taken out of its vessel and checked upon arrival the 20th of April. The vessel was leak and vacuum tested by the local ISIS crew [28]. This is necessary since any particles in the LET tank risk to scatter and deflect the neutrons between the

sample and the detector.

To test the functioning of the detector, after the detector vessel was OKd, a first test was performed. The detector and readout electronics were set up in the detector testing area and connected to low voltage, high voltage and Ar/Co2 gas supply. The first measurement was preformed using an AmBe source on the 22 of April. This AmBe source was not properly moderated in contrast to the AmBe source used at the STF. The indication after this first measurement was that the DAQ and detector was functioning [28], [29].

The detector was placed the the so-called quiet cave on the 22 of April. The quiet cave is a layered structure, with outer layers of polyethylene which thermalizes fast neutrons. Inner layers of Mirrobor™shields against thermalized neutrons [28]. The measurement was started and run until the 25 of April.

After the initial tests were completed the detector was deemed working and was moved into the LET detector vacuum tank on the 25 of April. The gas and readout electronics were connected, the high voltage was ramped up to 1100 V and the low voltage was applied. The DAQ was started the 26th of April and immediately it was noticed that empty channels connected to ground registered a lot of noises that overloaded the DAQ [30].

To check the detector it was opened up again, and while nothing as to why the problem had arisen, a loose high voltage cable was found and re-soldered into place. The detector was then closed again, and all electronics was reconnected. The problems with the noisy empty channels was remedied by raising the hardware discrimination threshold on the wires and by disregarding these channels at the software level.

To make sure the detector functioned as before with the new settings inside the LET tank the DAQ was started and run over night. Data collected over this period did not show anything unexpected and the detector was deemed to work. The LET tank was then pumped down towards vacuum to prepare for the beam-time. The DAQ was run continuously for several days to monitor the detector [31].

On the 4th of May, the first neutron beam was acquired. To confirm the detector alignment inside the LET cave the first sample used was a C_{60} sample, which scatters neutrons in all directions [32]. For the time of flight measurement a thin vanadium sample was used. The choppers were set to deliver neutrons with wavelengths 1.35 Å, 2.47 Å, 3.59 Å, 4.72 Å and 5.84 Å. Due to low statistics from the vanadium sample, a SiO_2 sample was used instead on the 5th of May.

The time-of-flight peaks, corresponding to neutron energy peaks, can be directly compared with the ^{3}He detector, specifically the line-shape as well as the signal to background ratio. The energy transfer spectra peaks (initial neutron energy minus the energy of the scattered neutron) is shown in figure 7.2. Observe that these spectra have been normalized to the number of counts in each peak. All Multi-Grid peaks match the ^{3}He detector peaks well. The width of the peaks are similar, as well as the signal to background ratio. One thing to note in figures 7.2 (b) and (c) is the shoulder to the right of the main peak. This has been observed in previous measurements with

previous Multi-Grid prototypes and is thought to originate from scattered neutrons within the detector [15]. All peaks are centered around 0 deposited energy, meaning these are elastic scattering peaks.

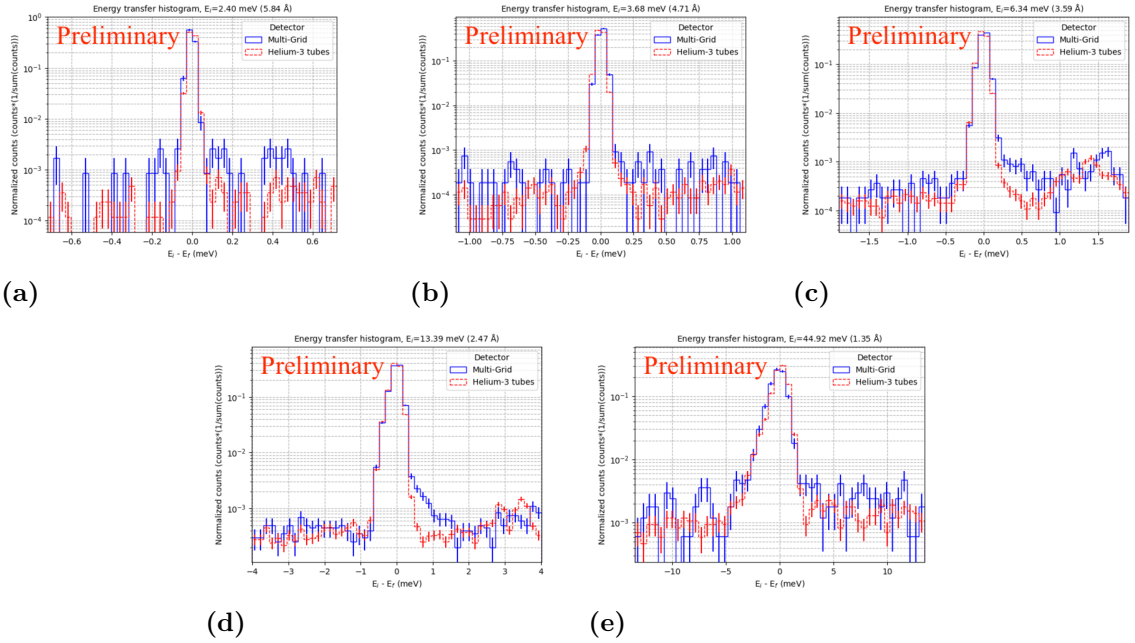

Figure 7.2: The energy transfer peaks from the neutron scattering from the vanadium and the SiO_2 samples, figures taken from [33] (note that these figures are preliminary and may be altered). (a) show the energy transfer peak for the neutrons with initial energy 44.92 meV (1.35 Å). (b) show the energy transfer peak for the neutrons with initial energy 13.39 meV (2.47 Å). (c) show the energy transfer peak for the neutrons with initial energy 6.34 meV (3.59 Å). (d) show the energy transfer peak with initial neutron energy 3.68 meV (4.71 Å). Lastly (e) show the energy transfer peak for the neutrons with initial energy 2.40 meV (5.84 Å).

The low statistics from the vanadium is thought to be due to impurities in the gas used inside the detector, this is still being investigated as of the time of writing this report.

From the experiment performed at LET preliminary results from the Multi-Grid data are promising in its likeness to the ^{3}He detector. Both the line-shape and the background to signal ratio is comparable for the two detector types. No quantitative comparisons between the detector types are possible at this stage and is left for further analyses.

However, if the shoulder observed in some of the energy transfer spectra is unresolved it may hide interesting features in the region near the quasi-elastic peak. This is of a concern to the CSPEC instrument and is currently under throughout investigation.

8 Summary and Conclusion

In this work one prototype of the Multi-Grid detector has been constructed at the ESS detector workshop Utgård, called the CSPEC Multi-Grid detector. The $^{10}B_4C$-coated aluminum blades used in Multi-Grid detectors were assembled into grids and welded. The grids were then stacked besides each-other on the detector backbone. The wires were then soldered into place and the detector was mounted into its aluminum vessel. The detector electronics were connected together with the Ar/Co_2 gas used.

The first tests were performed at Utgård and tested the initial functionality of the components of the constructed detector together with the data acquisition systems functionality, as well as any intrinsic background signals from the detector. These tests showed that all wires, but one, all grids and the DAQ were functioning. The tests did not indicate any problematic intrinsic background signals from the detector.

The detector was then moved to the STF and tested further. Here a gamma-ray source was used for a threshold calibration to discriminate against gamma-rays, since gamma-rays will be part off the background radiation at CSPEC, as well as a thermalized neutron source to get early indications on whether or not the detector is sensitive to neutrons. These tests indicated that gamma-rays were predominantly detected with low charge coincidence events, which provided an initial gamma-ray discrimination threshold at 550 adc to use in the software stage of data analyses. They also indicated that the detector is sensitive thermal neutrons, the efficiency is however not determined.

The detector was then shipped to ISIS where quantitative tests were performed at the LET instrument to compare the Multi-Grid detector to a ^{3}He detectors used in the LET instrument. These tests confirmed that the detector does detect thermal neutrons, furthermore it detects neutrons with energies relevant for the CSPEC instrument. They also indicated that the signal to background ratio as well as the line-shape from the detector was comparable to the ^{3}He detector.

In conclusion, in this work the CSPEC Multi-Grid detector have been constructed and tested. The tests have determined that all components of the detector, except one, as well as the DAQ was functioning. The tests also provided a first gamma-ray discrimination threshold, furthermore they showed that the detector detects neutrons in the energy range relevant for CSPEC with a line-shape and signal to background ratio comparable to the well-established ^{3}He detector.

Bibliography

[1] W. Lohstroh, W. Petry, J. Neuhaus, L. Silvi, C. Simionesco, J. Zanotti, S. Longeville and P. Deen. "ESS Instrument Construction Proposal CSPEC Cold chopper spectrometer". In: (2013).

[2] J. Lilley. *Nuclear Physics, Principles and Applications*. 1st ed. Chichester: Wiley & sons Ltd, 2001.

[3] Britannica and The Editors of Encyclopaedia. "neutron". In: *Encyclopedia Britannica* (). eprint: https://www.britannica.com/science/neutron.

[4] R. Pynn. "neutron scatteing A PRIMER". In: *LOS ALAMOS SCIENCE* 19 (1990). URL: https://la-science.lanl.gov/lascience19.shtml.

[5] M. Wulf Friedlander. "cosmic ray". In: *Encyclopedia Britannica* (). eprint: https://www.britannica.com/science/cosmic-ray.

[6] J. Scherzinger, J.R.M. Annand, G. Davatz, K.G. Fissum, U. Gendotti, R. Hall-Wilton, E. Håkansson, R. Jebali, K. Kanaki, M. Lundin, B. Nilsson, A. Rosborge and H. Svensson. "Tagging fast neutrons from an 241Am/9Be source". In: *Applied Radiation and Isotopes* 98 (2015), pp. 74–79. ISSN: 0969-8043. DOI: https://doi.org/10.1016/j.apradiso.2015.01.003. URL: https://www.sciencedirect.com/science/article/pii/S0969804315000044.

[7] G. Russel. "Spallation Physics - An Overview". In: 1st ed. Los Alamos, New Mexico: Los Alamos National Laboratory, 1990, p. 291.

[8] EUROPEAN SPALLATION SOURCE. "ESS revises project plan and budget". In: (2021).

[9] EUROPEAN SPALLATION SOURCE. "How It Works". In: (). URL: https://europeanspallationsource.se/accelerator/how-it-works. (accessed: 03.05.2022).

[10] EUROPEAN SPALLATION SOURCE. "How It Works". In: (). URL: https://europeanspallationsource.se/target/how-it-works. (accessed: 16.05.2022).

[11] K.H. Andersen et al. "The instrument suite of the European Spallation Source". In: *Nuclear Instruments and Methods in Physics Research Section A: Accelerators, Spectrometers, Detectors and Associated Equipment* 957 (2020), p. 163402. ISSN: 0168-9002. DOI: https://doi.org/10.1016/j.nima.2020.163402. URL: https://www.sciencedirect.com/science/article/pii/S0168900220300097.

[12] P. P. Deen, S. Longeville, W. Lohstroh, F. Moreira, G. Fabrèges, L. Loaiza and D. Noferini. "CSPEC: The cold chopper spectrometer of the ESS, a detailed overview prior to commissioning". In: *Review of Scientific Instruments* 92.10 (2021), p. 105104. DOI: 10.1063/5.0059907. eprint: https://doi.org/10.1063/5.0059907. URL: https://doi.org/10.1063/5.0059907.

[13] J. Correa Magdalena. "10B4C Multi-Grid as an Alternative to 3He for Large Area Neutron Detectors". In: (2013).

[14] M. Anastasopoulos, R. Bebb, K. Berry, J. Birch, T. Bryś, J.-C. Buffet, J.-F. Clergeau, P.P. Deen, G. Ehlers, P. van Esch, S.M. Everett, B. Guerard, R. Hall-Wilton, K. Herwig, L. Hultman, C. Höglund, I. Iruretagoiena, F. Issa, J. Jensen, A. Khaplanov, O. Kirstein, I. Lopez Higuera, F. Piscitelli, L. Robinson, S. Schmidt and I. Stefanescu. "Multi-Grid detector for neutron spectroscopy: results obtained on time-of-flight spectrometer CNCS". In: *Journal of Instrumentation* 12.04 (Apr. 2017), P04030–P04030. DOI: 10.1088/1748-0221/12/04/p04030. URL: https://doi.org/10.1088/1748-0221/12/04/p04030.

[15] A Backis, A Khaplanov, R Al Jebali, R Ammer, I Apostolidis, J Birch, C C Lai, P P Deen, M Etxegarai, N de Ruette, J Freita Ramos, D F Förster, E Haettner, R Hall-Wilton, D Hamilton, C Höglund, P M Kadletz, K Kanaki, E Karnickis, O Kirstein, S Kolya, Z Kraujalyte, A Laloni, K Livingston, O Löhman, V Maulerova, N Mauritzon, F Müller, I Lopez Higuera, T Richter, L Robinson, R Roth, M Shetty, J Taylor, R Woracek and W Xiong. "Time- and energy-resolved effects in the boron-10 based multi-grid and helium-3 based thermal neutron detectors". In: *Measurement Science and Technology* 32.3 (Dec. 2020), p. 035903. DOI: 10.1088/1361-6501/abc63e. URL: https://doi.org/10.1088/1361-6501/abc63e.

[16] Francesco Piscitelli. "Boron-10 layers, Neutron Reflectometry and Thermal Neutron Gaseous Detectors". PhD thesis. Jan. 2014.

[17] A. Backis, A. Carmona, F. Piscitelli and J. Isabelle. *Detector Efficiency Calculator*. URL: https://github.com/ess-dg/dg_efficiencyCalculator. (accessed: 9.06.2022).

[18] Á. Basánez, K. Kanaki and F. Piscitelli. *DECal, a Python tool for the efficiency calculation of thermal neutron detectors based on thin-film converters*. URL: https://arxiv.org/pdf/1801.07124.pdf. (accessed: 9.06.2022).

[19] Takatomi Yano. "Measurement of gamma-ray production from thermal neutron capture on gadolinium for neutrino experiments". In: *Nuclear Instruments and Methods in Physics Research Section A: Accelerators, Spectrometers, Detectors and Associated Equipment* 845 (2017). Proceedings of the Vienna Conference on Instrumentation 2016, pp. 425–428. ISSN: 0168-9002. DOI: https://doi.org/10.1016/j.nima.2016.06.084. URL: https://www.sciencedirect.com/science/article/pii/S0168900216306477.

[20] MIRROTRON. *Radiation Shielding Neutron Shielding: Mirrobor ™*. URL: https://mirrotron.com/en/products/radiation-shielding. (accessed: 27.05.2022).

[21] Mesytec GmbH & Co. KG. *Vmmr-8/16*. URL: www.mesytec.com/products/datasheets/VMMR.pdf. (accessed: 23.05.2022).

[22] H. Perrey and K. Fissum. *Source Testing Facility*. URL: https://portal.research.lu.se/sv/equipments/source-testing-facility. (accessed: 02.05.2022).

[23] J. Scherzinger, R. Al Jebali, J.R.M. Annand, K.G. Fissum, R. Hall-Wilton, S. Koufigar, N. Mauritzson, F. Messi, H. Perrey and E. Rofors. "A comparison of untagged gamma-ray and tagged-neutron yields from 241AmBe and 238PuBe sources". In: *Applied Radiation and Isotopes* 127 (2017), pp. 98–102. ISSN: 0969-8043. DOI: https://doi.org/10.1016/j.apradiso.2017.05.014. URL: https://www.sciencedirect.com/science/article/pii/S0969804316309861.

[24] F. Messi, H. Perrey et al. “The neutron tagging facility at Lund University”. In: *Modern Neutron Detection*. TECDOC Series 1935. Vienna: INTERNATIONAL ATOMIC ENERGY AGENCY, 2020, 287–297. ISBN: 978-92-0-126520-3. eprint: https://arxiv.org/abs/1711.10286. URL: https://www.iaea.org/publications/14690/modern-neutron-detection.

[25] V. Maulerová. “Vanadium-based neutron-beam monitor”. In: (2019). Thesis submitted for the degree of Master of Science.

[26] Science and Technology Facilities Council. *How ISIS works*. URL: https://www.isis.stfc.ac.uk/Pages/How-ISIS-works.aspx. (accessed: 02.05.2022).

[27] Science and Technology Facilities Council. *LET*. URL: https://www.isis.stfc.ac.uk/Pages/Let.aspx. (accessed: 02.05.2022).

[28] N. A. Backis. *Week 1: 20/4-22/4*. URL: https://stf01.nuclear.lu.se/MG.CSPEC/251. (accessed: 26.05.2022).

[29] N. A. Backis. *AmBe-measurements: 22/4-2022*. URL: https://stf01.nuclear.lu.se/MG.CSPEC/253. (accessed: 01.06.2022).

[30] N. A. Backis. *First tests in LET tank: 25/6-2022 and 26/6-2022*. URL: https://stf01.nuclear.lu.se/MG.CSPEC/254. (accessed: 01.06.2022).

[31] N. A. Backis. *LET tank in vacuum, no beam: 27/4-2022*. URL: https://stf01.nuclear.lu.se/MG.CSPEC/256. (accessed: 01.06.2022).

[32] N. A. Backis. *Multi-Grid detector: white beam on C60 (”buckyballs”) sample*. URL: https://stf01.nuclear.lu.se/MG.CSPEC/266. (accessed: 01.06.2022).

[33] N. A. Backis. *Introducing tof cuts for each peak*. URL: https://stf01.nuclear.lu.se/MG.CSPEC/280. (accessed: 01.06.2022).

Appendix A

Contribution list

Below, the contributions of the auther of this work is stated.

A Garfield ++ simulation was performed by me, through defining the gas inside the detector, together with the geometry of a cell with set electric potentials, and choosing a the plotting options.

I assembled 36 grids in total, welded 76 grids and soldered about 100 to 150 wires. 20 of the grids in the reference detector was also put in place by me. I also cut up 7 sheets of Gd_2O_3 shielding as well as glued 17 aluminum back pieces of the grid to cut Gd_2O_3 shielding pieces. As might be noted the reference detector only has 37 grids, while I welded more than that. The reason behind this was that the Multi-Grid detector was built in parallel to another prototype of the Multi-Grid detector which I also helped to build. I did not build the reference detector by my self, we were a group of people that built the reference detector in the same time as we built another prototype.

I checked the grid PCB signaling with a multi-meter as well as a grid PCB for the sequoia detector to compare how the corresponding channels will end up in the data analyses. The setup at Utgård was done previously, not by me. However, I did help connect all electronics and gas, inside and outside of the vessel. The first measurements taken at Utgård were started, stopped and analyzed by me.

Before moving the detector from Utgård to the STF, me and Alexander Backis planed what needed to be brought, and packed necessary wires and electronics to bring to the STF. The moving of the detector from Utgård to STF was done by Ramsey Al Jebali, Alessio Laloni and Alexander Backis. Me and Alexander Backis checked the detector at the STF, and together with Ramsey Al Jebali we connected all electronics, in the exact same way it was connected at Utgård.

Some measurements performed at the STF was also started, stopped and analyzed by me. Some measurements were stared and stopped by Ramsey Al Jebali. Several Elog entries were written by me of the STF measurements.

The code used to obtain coincidence events were based on Alexander Backis code but had to be rewritten to fit the exact setup of this detector. The code used to plot the images in the analyses section is also based on Alexander Backis code but is rewritten to better fit the scope of this work.

I arrived at ISIS the 27 of April and my last day was the 5 of May. During my time at ISIS I mostly contributed by being part of the discussion on the preliminary results. I did not touch the detector at all during my visit. All analyses performed at ISIS and

after ISIS was and is done by Alexander Backis.

Appendix B

Grid configurations

In this section the three grid configurations are showed. There are two thicknesses of the $^{10}B_4C$-coating on the normal blades: $0.65\,\mu$m (noted 065 in the figures) and $1.15\,\mu$m (noted 115 in the figures). NB stands for normal blades; ORB stands for outer radial blades and IRB stand for inner radial blades. The radial blades are all double coated with $2\,\mu$m thick $^{10}B_4C$-coating. All blades are given a letter, this is due to the varying thickness of $^{10}B_4C$-coating on the blades. Three blades are handled simultaneously, these are then called top (T), center (C) and bottom (B) blades. The center blade has a more even thickness of $^{10}B_4C$-coating compared to the top and bottom blades. To even out the effect of this, the top and bottom blades are used every other time.

To maximize the neutron capture efficiency a thinner layer of coating is used towards the front of the grid, compared to the back of the grid. Three configurations were made to be able to study if any configuration has a higher neutron detection efficiency.

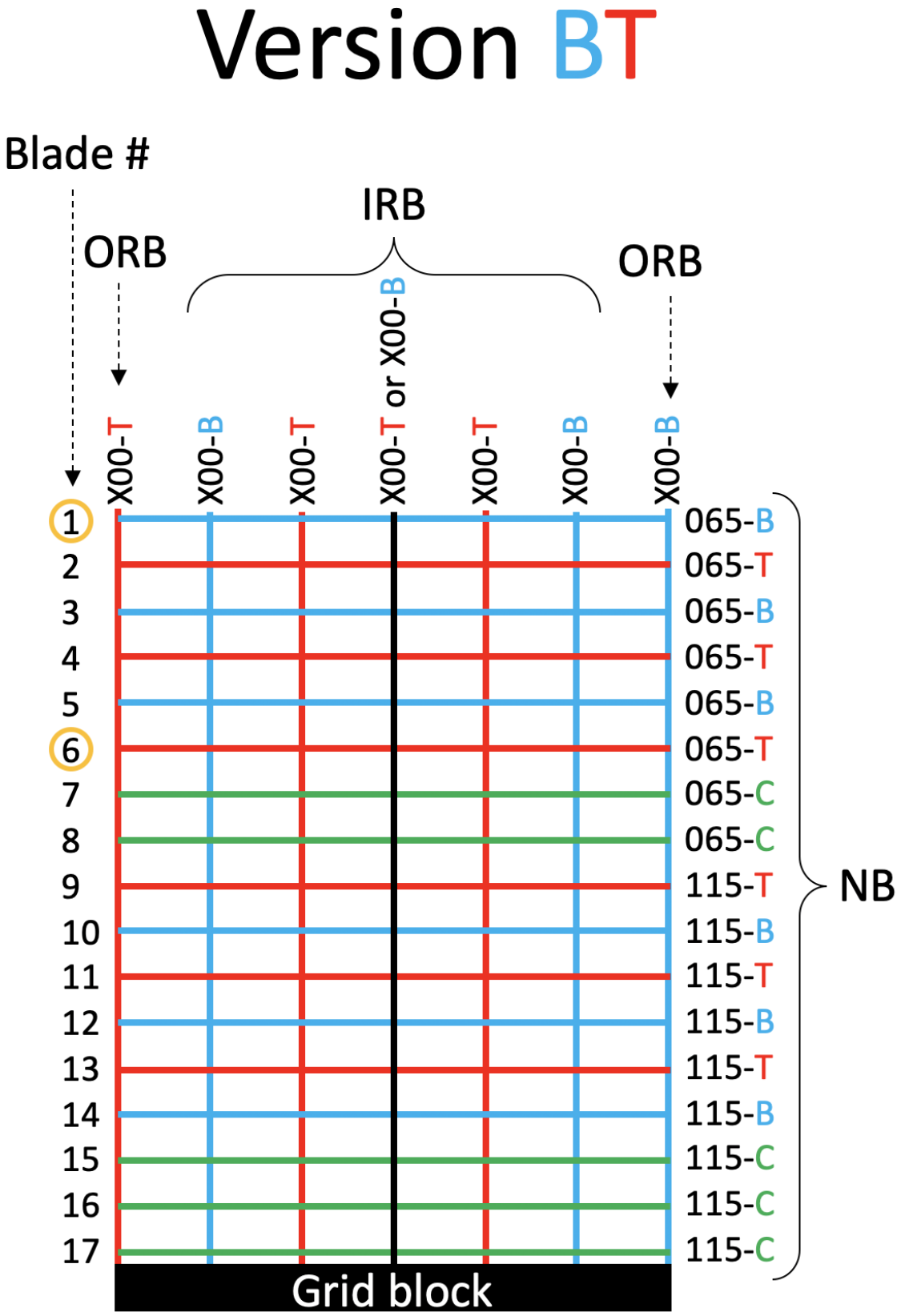

Figure B.1: The BT grid configuration. Image aquired from Alexander Backis at the detector group of ESS

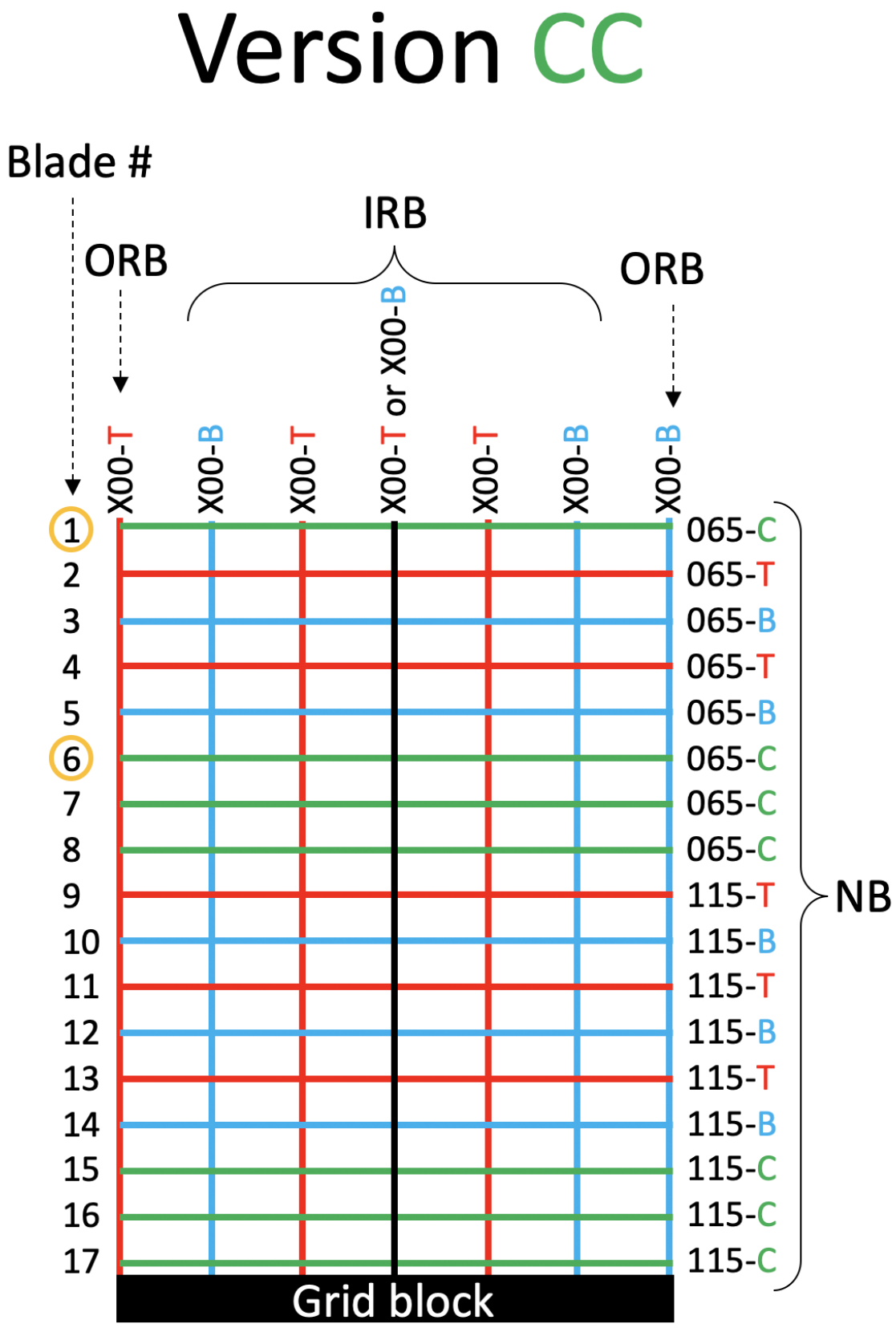

Figure B.2: The CC grid configuration. Image aquired from Alexander Backis at the detector group of ESS

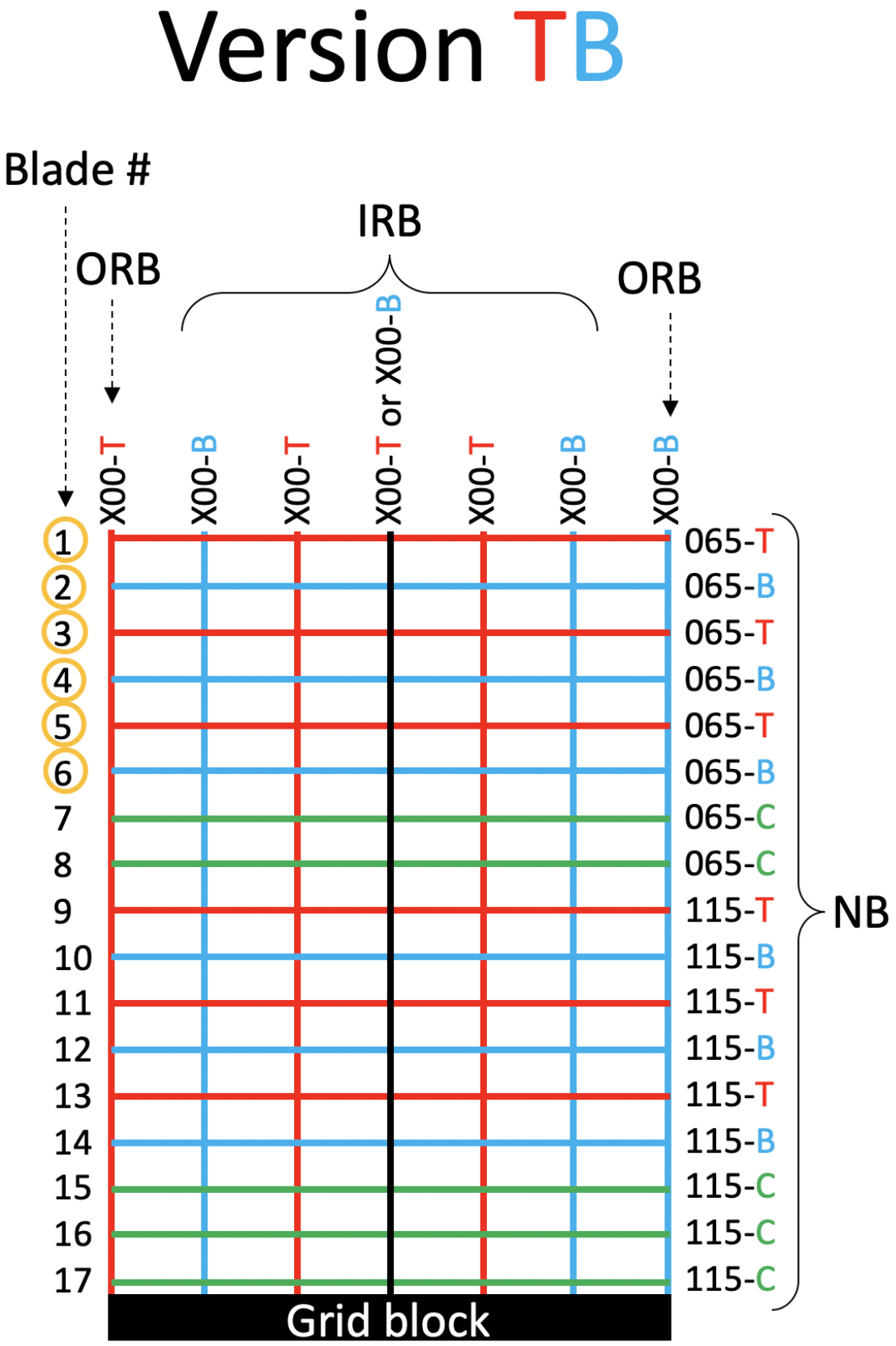

Figure B.3: The TB grid configuration. Image aquired from Alexander Backis at the detector group of ESS